

Durham Research Online

Deposited in DRO:

28 April 2020

Version of attached file:

Accepted Version

Peer-review status of attached file:

Peer-reviewed

Citation for published item:

Gong, Y. and Dong, C. and Qin, F. and Hattori, G. and Trevelyan, J. (2020) 'Hybrid nearly singular integration for three-dimensional isogeometric boundary element analysis of coatings and other thin structures.', *Computer methods in applied mechanics and engineering*, 367 . p. 113099.

Further information on publisher's website:

<https://doi.org/10.1016/j.cma.2020.113099>

Publisher's copyright statement:

© 2020 This manuscript version is made available under the CC-BY-NC-ND 4.0 license
<http://creativecommons.org/licenses/by-nc-nd/4.0/>

Additional information:

Use policy

The full-text may be used and/or reproduced, and given to third parties in any format or medium, without prior permission or charge, for personal research or study, educational, or not-for-profit purposes provided that:

- a full bibliographic reference is made to the original source
- a [link](#) is made to the metadata record in DRO
- the full-text is not changed in any way

The full-text must not be sold in any format or medium without the formal permission of the copyright holders.

Please consult the [full DRO policy](#) for further details.

Hybrid nearly singular integration for three-dimensional isogeometric boundary element analysis of coatings and other thin structures

Yanpeng Gong^{a,*}, Chunying Dong^b, Fei Qin^a, Gabriel Hattori^c, Jon Trevelyan^d

^a*College of Mechanical Engineering and Applied Electronics Technology, Beijing University of Technology, Beijing, 100124, China*

^b*Department of Mechanics, School of Aerospace Engineering, Beijing Institute of Technology, Beijing, 100081, China*

^c*Department of Engineering, University of Cambridge, Civil Engineering Building, Cambridge, CB3 0FA, UK*

^d*Department of Engineering, Durham University, Durham, DH1 3LE, UK*

Abstract

The isogeometric boundary element method (IGABEM) has great potential for the simulation of elasticity problems because of its exact geometric representation and good approximation properties. These advantages can be extended to thin structures, including coatings, but the development of an accurate and efficient method to deal with the large number of nearly singular integrals existing in the IGABEM presents a great challenge for very thin sections. In this paper, we propose a new \sinh^+ scheme for weakly, strongly and hyper near-singular integrals arising in 3D IGABEM for thermoelastic problems, based on the \sinh transformation method and adaptive integral method. The presented scheme is efficient, since it combines the advantages of both methods: (1) when the thickness δ of coatings/thin structures is moderately small, an accurate and efficient integral result will be obtained by the adaptive integral method; (2) when δ is very small, the nearly singular integrals are computed by the \sinh^+ scheme efficiently. With the introduction of NURBS in IGABEM, truncation errors arising in the Taylor expansion cannot be ignored. Based on the values of these errors, the computed knot spans are further divided into several sub-knot spans and different methods will be used to evaluate the integral over each sub-knot span in the new scheme. In addition, based on the analytical extension of the NURBS surface, an adaptation of the \sinh transformation method is proposed which can evaluate the near-singular integrals accurately for cases in which the projection point lies outside of the considered knot span. Several numerical examples are presented to validate the accuracy and efficiency of the 3D IGABEM based on the \sinh^+ scheme in the analysis of thermoelastic problems.

Keywords: Boundary element method, Isogeometric analysis, Surface nearly singular integrals, Thermoelastic problem, Coatings/thin structure.

1. Introduction

Coatings or other thin structures have been widely used to protect a variety of structural engineering materials from corrosion, wear, and erosion, and to provide lubrication and thermal insulation [1, 2]. The great difference in the thermo-mechanical properties of substrate and coatings presents challenges to their use in composite structures subjected to large changes in temperature. In the past two decades, significant research effort has been devoted to the analysis and development of thermal barrier coatings (TBCs) on engineering problems since more traditional coating materials have reached the limits of their temperature capabilities [3].

*Corresponding author.

Email addresses: yanpeng.gong@bjut.edu.cn (Yanpeng Gong), cydong@bit.edu.cn (Chunying Dong), qfei@bjut.edu.cn (Fei Qin), gh465@cam.ac.uk (Gabriel Hattori), jon.trevelyan@durham.ac.uk (Jon Trevelyan)

Many experimental, analytical and numerical methods are available to study the mechanics of coatings or thin structures. For example, Evans and Hutchinson presented the mechanics of delamination in coatings that experience thermal gradients [4]. Based on the higher-order theory for functionally graded materials (FGMs), Pindera et al. [5] analysed the spalling mechanism in TBCs with graded bond coats. The Finite Element Method (FEM) is a powerful method for the analysis of many engineering problems and has been applied to study coatings by many researchers, including Białas [6] who studied the stress distribution in TBCs, and Skalka et al. [7] who studied the effect of the waviness of the bond coat and the thickness of the thermally grown oxide layer on the stability of plasma-sprayed thermal barrier coatings through a large number of 3D finite element calculations. Through commercial software (ABAQUS and CATIA), Yang et al. [8] developed finite element approximations to investigate the failure behavior of TBCs under cyclic thermal loading. However, as the aspect ratio reduces, the number of elements required in the FEM increases dramatically, and the procedure becomes time-consuming for coatings having small thickness. Although shell elements can be used to analyse some thin sections, it is desirable to have a better description of the solution variation through the thickness direction.

Since the geometric representations in traditional finite element analysis and Computer Aided Design (CAD) are different, a computational burden is involved in providing an interface between these technologies in the process of Computer Aided Engineering (CAE). In 2005, Hughes et al. proposed the “Isogeometric Analysis” (IGA) paradigm [9] as a means to perform finite element analysis directly from CAD data, for three-dimensional regions. Actually, the first paper known to the authors to propose approximations that are today called “isogeometric” dates back to 1982 [10], although this was significantly different from the approach presented by Hughes et al. [9]. Isogeometric schemes involve the substitution of the classical piecewise polynomial description of the geometry and solution by an expansion in Non-Uniform Rational B-Splines (NURBS). This brings three key advantages that have been widely discussed in the literature. Firstly, it allows more direct integration with CAD systems that use this geometric description and therefore allows exact geometric representations of conic sections. Secondly, the process of meshing is replaced by simple knot-insertion and/or degree elevation algorithms. And thirdly, it is found that the smoothness of the NURBS basis functions offers the improved approximation properties in comparison with piecewise polynomial descriptions.

However, due to the use of NURBS, some difficulties exist in the original version of IGA. These difficulties are: (i) the performance of local refinement [11], (ii) an automatic parameterisation to build the approximation, (iii) enforcement of multi-patch constraints, and (iv) the need for an interior parameterisation to be constructed from the CAD data, which only provides boundary information [12]. Several methods were later devised in order to alleviate the difficulties faced by IGA [13–15]. And more details about IGA can be found in review papers [16–19]. Finally, researchers realised that Isogeometric Boundary Element Methods (IGABEM) [20, 21] are probably the best suited candidates to overcome the interior discretisation obstacle, since only boundary data is required for analysis without any mesh generation [22]. Afterwards, IGABEM was widely used for many applications, such as damage tolerance assessment of complex structures [23], acoustic problems [24] and fracture simulations [25].

The Boundary Element Method (BEM) is a powerful and efficient method for solving many engineering problems, offering an alternative to the FEM for a range of engineering simulations, with particular strengths in fracture mechanics, acoustic problems and infinite domain problems [26]. The main advantages of the BEM derive from the fact that its approximations (and mesh) only occur on the boundary, the dimension of the numerical model therefore being one less than that of the physical problem being modelled, and from the high accuracy of its solutions on comparatively coarse meshes. These advantages suggest the BEM should become an efficient tool in the analysis of coatings and thin structures [27–32]. However, the BEM analysis of solids has classically been restricted to problems without thin sections because such geometries impose a requirement to evaluate a large number of nearly-singular integrals accurately and efficiently. With the development of suitable integration schemes, the BEM has become an attractive method for coated structures and other thin sections, as demonstrated by [33] for the classical (piecewise polynomial) BEM in 2D and extended to isogeometric BEM by Gong et al. [2].

The advantages of isogeometric methods found in the FEM extend readily to elastic analysis with the BEM, and this was first demonstrated by Simpson et al. [20]. The resulting analysis method is called IGA-

BEM (isogeometric analysis boundary element method). The properties of exact geometric description and accurate computation of quantities along the thickness direction inside coatings or thin structures, suggest that IGABEM is a highly promising approach to study the coatings/thin structures [2, 20, 34]. However, schemes for the efficient and accurate evaluation of the near-singular integrals that arise in IGABEM need to be developed to realise this promise.

For the computation of near-singular integrals existing in standard BEM, significant progress has been achieved, including analytical methods [35–38], semi-analytical integration schemes [39, 40], cubic transformation [41], radial variable transformation [42], line integral approaches [43, 44], implemented method [45], parameterized Gaussian quadrature [46], the particular solution method [47, 48], adaptive integration schemes [49, 50], regularisation techniques [51, 52], domain supplemental approach [53], distance transformation method [54, 55], spherical element subdivision method [56], sinh transformation method [57–60], and the exponential transformation method [61, 62]. A more detailed review of these methods can be found in Gong et al. [2]. With the adoption of NURBS in IGABEM to replace simple polynomials, some of these methods cannot be applied directly; moreover, the balance between accuracy and efficiency of these methods when applied within a 3D IGABEM context is not yet clear.

In this work, we develop a scheme for 3D integrals based on the \sinh^+ scheme presented for 2D simulations in [2]; this combines the benefits of the sinh transformation [57–60] and adaptive integration scheme [49, 50]. An essential feature of the method is its ability to produce accurate and efficient integral evaluations for general, industrially relevant IGABEM models of thin sections or components with coatings. The resulting 3D \sinh^+ scheme is developed based on 3D thermoelastic integral equations, which involves weakly, strongly and hyper near-singular kernels (with orders $1/r$, $1/r^2$ and $1/r^3$, where r is the distance between the source/internal point and the field point). In the present \sinh^+ scheme, the parametric representation of the field point is expressed as a Taylor expansion (with two parameters ξ and η used in the NURBS definitions in the two coordinate directions of the element or knot-span), this expansion being taken around projection point of the source/internal point. In the new \sinh^+ scheme, the isogeometric element (knot span over which the integral is taken) will be divided into several sub-elements (sub-knot spans) according to the truncation errors of the Taylor series, and different integration methods will be adopted for different sub-elements. For the knot spans for which truncation errors exceed a prescribed tolerance, the adaptive integral method will provide the best balance between accuracy and efficiency. Conversely, for knot spans over which truncation errors are smaller than that tolerance, the sinh transformation method will be used to reduce the computation time of nearly singular integrals. To evaluate the near-singular integrals for cases in which the projection point of the collocation/internal point lies outside the considered isogeometric element, an extended sinh transformation on the field element is proposed.

The content of the paper is outlined as follows. In Section 2, a brief review of the BEM and IGABEM for thermoelastic problems is given. Section 3 introduces several numerical integration methods commonly used for nearly singular integrals and presents an analysis of the errors and efficiency of these methods. Based on the analytical extension of the bi-variable NURBS, Section 4 presents a new adaptation of the sinh transformation for isogeometric surface elements, including the case when the projection of the collocation/internal point lies outside the interval of integration. Section 5 presents the hybrid integration scheme, called the \sinh^+ scheme, for all the nearly singular integrals arising in 3D IGABEM for thermoelastic problems. Section 7 shows several numerical examples verifying the effectiveness of the present method. The paper is concluded with some discussions and closing remarks.

2. Boundary element method and isogeometric boundary element method

2.1. Boundary integral equations in thermoelasticity

In this section, we will outline the fundamentals of the BEM and IGABEM for 3D steady-state thermoelastic problems. For these problems, the structure occupies a continuous physical domain, $\Omega \subset \mathbb{R}^3$, with closed boundary Γ . It is assumed for simplicity in this paper that the domain is free of thermal sources/sinks in the heat transfer problem and inertial loads in the elasticity problem. It should not be interpreted from

this assumption that the methods cannot be used for cases in which body forces apply; it is simply a matter of presenting the material concisely. The governing equations for isotropic materials are [63]:

$$\begin{cases} \mu u_{i,jj} + \frac{\mu}{(1-2\nu)} u_{j,ji} - \frac{2\mu(1+\nu)}{1-2\nu} \alpha \Delta \theta_{,i} = 0 \\ k \theta_{,ii} = 0 \end{cases} \quad (1)$$

where μ is the shear modulus, E and ν are Young's modulus and Poisson's ratio, respectively, k is the thermal conductivity, and α is the thermal expansion coefficient. Parameters u and θ denote displacement and temperature, respectively. Subscripts $i, j = 1, 2, 3$ denote the coordinate directions in 3D problems. For heat transfer problems, the flux density in a direction x_i , denoted q_i , is defined as $q_i = k \partial \theta / \partial x_i$, and the normal flux density at a boundary, usually represented by q (without a subscript), and which is used in the definition of Neumann boundary conditions, is defined as

$$q = -k \frac{\partial \theta}{\partial \mathbf{n}} \quad (2)$$

105 where \mathbf{n} is the outward pointing normal. The negative sign is required so that the direction of the flux corresponds to flow of heat from regions of higher temperature to lower temperature.

Equation (1) is solved subject to a set of boundary conditions taken from the following:

$$u_i = \bar{u}_i \text{ on } \Gamma_{\bar{u}_i} \subset \Gamma \quad (3)$$

$$t_i = \bar{t}_i \text{ on } \Gamma_{\bar{t}_i} \subset \Gamma \quad (4)$$

$$\theta = \bar{\theta} \text{ on } \Gamma_{\bar{\theta}} \subset \Gamma \quad (5)$$

$$q = \bar{q} \text{ on } \Gamma_{\bar{q}} \subset \Gamma \quad (6)$$

110 where the quantities $\bar{u}_i, \bar{t}_i, \bar{\theta}$ and \bar{q} are known displacement, traction, temperature and flux density; t_i denotes the traction component in direction i ; $\Gamma_{\bar{u}_i}, \Gamma_{\bar{t}_i}, \Gamma_{\bar{\theta}}$ and $\Gamma_{\bar{q}}$ denote the parts of Γ over which displacement, traction, temperature and flux density are prescribed in each specific direction with $\Gamma_{\bar{u}_i} \cup \Gamma_{\bar{t}_j} = \Gamma$ ($\Gamma_{\bar{u}_i} \cap \Gamma_{\bar{t}_j} = \emptyset, i \neq j$) and $\Gamma_{\bar{\theta}} \cup \Gamma_{\bar{q}} = \Gamma$ ($\Gamma_{\bar{\theta}} \cap \Gamma_{\bar{q}} = \emptyset$).

For a 3D thermoelastic problem, the corresponding boundary integral equation (BIE) can be written as [64]

$$C_{ij}(\mathbf{y}) u_i(\mathbf{y}) + \int_{\Gamma} T_{ij}(\mathbf{y}, \mathbf{x}) u_j(\mathbf{x}) d\Gamma(\mathbf{x}) = \int_{\Gamma} U_{ij}(\mathbf{y}, \mathbf{x}) t_j(\mathbf{x}) d\Gamma(\mathbf{x}) + \frac{\alpha E}{1-2\nu} \int_V \frac{\partial U_{ij}(\mathbf{y}, \mathbf{x}')}{\partial x_j} \theta(\mathbf{x}') dV(\mathbf{x}') \quad (7)$$

where $\mathbf{x}' \in \Omega$. Boundary points $\mathbf{y} \in \Gamma$ and $\mathbf{x} \in \Gamma$ are called the source point and field point, respectively, with \mathbf{y} playing the role of a collocation point. We note that the algorithms presented herein are not designed for Galerkin BEM formulations, but a scheme could be derived using the same principles. T_{ij} and U_{ij} are the displacement and traction fundamental solutions (or kernels). C_{ij} is the jump term which is commonly calculated indirectly by using a simple physical consideration [64, 65]. The displacement and traction fundamental solutions in 3D for isotropic materials are given as [64]

$$U_{ij} = \frac{1}{16\pi\mu(1-\nu)r} [(3-4\nu)\delta_{ij} + r_{,i}r_{,j}] \quad (8)$$

$$T_{ij} = \frac{-1}{8\pi(1-\nu)r^2} \left\{ \frac{\partial r}{\partial \mathbf{n}} [(1-2\nu)\delta_{ij} + 3r_{,i}r_{,j}] + (1-2\nu)(r_{,j}n_i - r_{,i}n_j) \right\} \quad (9)$$

where $r = r(\mathbf{y}, \mathbf{x}) = \|\mathbf{y} - \mathbf{x}\|$ is the distance between the source point and the field point, given by

$$r(\mathbf{y}, \mathbf{x}) = \sqrt{(x_1 - y_1)^2 + (x_2 - y_2)^2 + (x_3 - y_3)^2}, \quad (10)$$

$r_{,i} = \frac{\partial r}{\partial x_i}$, and n_i is the i th component of the unit outward normal vector \mathbf{n} to the boundary surface at the field point \mathbf{x} .

The existence of a volume integral term in an integral equation causes the BEM to lose its advantage of having only boundary integrals, but there are several methods available to transform domain integrals (in Eq. (7)) into equivalent boundary integrals [64, 66–69]. The resulting BIE for the thermoelastic problem can be expressed as follows:

$$C_{ij}(\mathbf{y})u_i(\mathbf{y}) + \int_{\Gamma} T_{ij}(\mathbf{y}, \mathbf{x})u_j(\mathbf{x})d\Gamma(\mathbf{x}) = \int_{\Gamma} U_{ij}(\mathbf{y}, \mathbf{x})t_j(\mathbf{x})d\Gamma(\mathbf{x}) + \int_{\Gamma} M_i(\mathbf{y}, \mathbf{x})\theta(\mathbf{x})d\Gamma(\mathbf{x}) + \int_{\Gamma} N_i(\mathbf{y}, \mathbf{x})\frac{\partial\theta(\mathbf{x})}{\partial\mathbf{n}}d\Gamma(\mathbf{x}) \quad (11)$$

where the kernels M_i and N_i , derived from the volume integral, can be expressed as

$$M_i(\mathbf{y}, \mathbf{x}) = \frac{\alpha(1+\nu)}{8\pi(1-\nu)} \frac{1}{r(\mathbf{y}, \mathbf{x})} \left[n_i(\mathbf{x}) - \frac{\partial r(\mathbf{y}, \mathbf{x})}{\partial x_i} \frac{\partial r(\mathbf{y}, \mathbf{x})}{\partial \mathbf{n}} \right] \quad (12)$$

$$N_i(\mathbf{y}, \mathbf{x}) = -\frac{\alpha(1+\nu)}{8\pi(1-\nu)} \frac{\partial r(\mathbf{y}, \mathbf{x})}{\partial x_i} \quad (13)$$

Eq. (11) is a displacement BIE one might use to solve a thermoelastic problem given a known distribution of temperature θ and flux density q . These quantities can be used directly if they are known, but the more usual situation is that they need to be computed from a heat transfer analysis in which the governing partial differential equation is solved subject to certain boundary conditions. For the current work this is most sensibly done using another boundary element model. The following BIE is standard for the steady state thermal problem,

$$C(\mathbf{y})\theta(\mathbf{y}) + \int_{\Gamma} Q(\mathbf{y}, \mathbf{x})\theta(\mathbf{x})d\Gamma(\mathbf{x}) = \int_{\Gamma} \Theta(\mathbf{y}, \mathbf{x})q(\mathbf{x})d\Gamma(\mathbf{x}) \quad (14)$$

where $\mathbf{x} \in \Gamma$ and $\mathbf{y} \in \Gamma$ are the field point and source point, respectively. $\Theta(\mathbf{y}, \mathbf{x})$ and $Q(\mathbf{y}, \mathbf{x})$ represent the temperature and flux fundamental solution kernels, and $C(\mathbf{y})$ is the jump term. The temperature and flux fundamental solutions in 3D for isotropic materials are given as

$$\Theta(\mathbf{y}, \mathbf{x}) = -\frac{1}{4\pi r} \quad (15)$$

$$Q(\mathbf{y}, \mathbf{x}) = \frac{\partial\Theta(\mathbf{y}, \mathbf{x})}{\partial\mathbf{n}(\mathbf{x})} \quad (16)$$

2.2. Description of boundary geometry

The BEM in 3D simulations requires a surface description of the boundary, and this is conveniently achieved using patches as illustrated in Figure 1. On the basis of the description of NURBS surface in [70, 71], mapping from the local parameter space (ξ, η) to physical space (global coordinate system, $\mathbf{x} \in \mathbb{R}^3$) can be expressed as

$$\mathbf{x}(\xi, \eta) = \sum_{a=1}^n \sum_{b=1}^m R_{ab}(\xi, \eta) \mathbf{P}_{ab} \quad (17)$$

where \mathbf{P}_{ab} ($a = 1, 2, \dots, n$, $b = 1, 2, \dots, m$) denotes the set of control net coordinates. $R_{ab}(\xi, \eta)$ are NURBS basis functions defined by [70, 71]

$$R_{ab}(\xi, \eta) = \frac{N_{a,p}(\xi)N_{b,q}(\eta)w_{ab}}{W(\xi, \eta)} \quad (18)$$

with

$$W(\xi, \eta) = \sum_{a=1}^n \sum_{b=1}^m N_{a,p}(\xi)N_{b,q}(\eta)w_{ab} \quad (19)$$

where $N_{a,p}(\xi)$ and $N_{b,q}(\eta)$ are univariate B-spline basis functions of orders p and q , corresponding to knot vectors $\Xi = \{\xi_1, \xi_2, \dots, \xi_{n+p+1}\}$ and $\mathcal{H} = \{\eta_1, \eta_2, \dots, \eta_{m+q+1}\}$, respectively. w_{ab} denotes a weight associated with control point \mathbf{P}_{ab} .

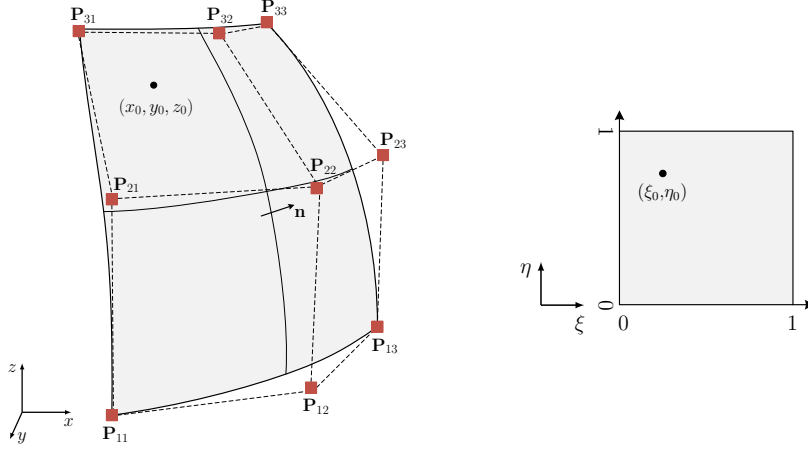


Figure 1: Example of a patch for 3D simulation with control net (numbered red squares). Left: in the global coordinate system (\mathbb{R}^3), Right: in the local coordinate system (\mathbb{R}^2).

2.3. Approximation of physical quantities

The fundamental concept behind isogeometric analysis methods is that the same basis functions (NURBS) are used to approximate the solution variables as well as describing the geometry. As with the geometrical mapping in Eq. (17), the physical quantities u^h within a patch can be interpolated through NURBS approximation as follows [9, 71]:

$$u^h(\xi, \eta) = \sum_{a=1}^n \sum_{b=1}^m R_{ab}(\xi, \eta) d_{ab} \quad (20)$$

Due to the non-interpolatory property of the NURBS, the terms d_{ab} cannot be considered to be nodal values, indeed we no longer have nodes as would be used in classical BEM techniques. Instead the terms d_{ab} , which will be found in the main solution vector, are coefficients from which the solution quantity can be recovered from Eq. (20).

2.4. Implementation of 3D IGABEM for thermoelastic problem

There are several differences between conventional BEM and IGABEM, such as the type of basis functions, location of collocation points, and application of boundary conditions. Since we no longer have elements defined by nodal positions and connectivity, it is convenient to think of an isogeometric ‘element’ as being that portion of the boundary enclosed within a knot span, and this is useful in practice for implementation of schemes for the evaluation of the boundary integrals required. Such a knot span is defined parametrically as $[\xi_i, \xi_{i+1}] \times [\eta_j, \eta_{j+1}]$, where $\xi_i, \xi_{i+1} \in \Xi$ and $\eta_j, \eta_{j+1} \in \mathcal{H}$. Through knot spans, the boundary surface of computation models can be discretized into several elements (Γ_e , $e = 1, 2, \dots, N_e$). Making use of the general expression (20), the displacement $\mathbf{u} = (u_1, u_2, u_3)^T$, traction $\mathbf{t} = (t_1, t_2, t_3)^T$, temperature θ and flux density q fields in an isogeometric element can be expressed using a NURBS expansion, i.e.

$$\mathbf{u}(\xi, \eta) = \sum_{a=1}^{p+1} \sum_{b=1}^{q+1} R_{ab}(\xi, \eta) \tilde{\mathbf{u}}_{ab} \quad (21)$$

$$\mathbf{t}(\xi, \eta) = \sum_{a=1}^{p+1} \sum_{b=1}^{q+1} R_{ab}(\xi, \eta) \tilde{\mathbf{t}}_{ab} \quad (22)$$

$$\theta(\xi, \eta) = \sum_{a=1}^{p+1} \sum_{b=1}^{q+1} R_{ab}(\xi, \eta) \tilde{\theta}_{ab} \quad (23)$$

$$q(\xi, \eta) = \sum_{a=1}^{p+1} \sum_{b=1}^{q+1} R_{ab}(\xi, \eta) \tilde{q}_{ab} \quad (24)$$

where $\tilde{\mathbf{u}}_{ab} = (\tilde{u}_1, \tilde{u}_2, \tilde{u}_3)^T$, $\tilde{\mathbf{t}}_{ab} = (\tilde{t}_1, \tilde{t}_2, \tilde{t}_3)^T$, $\tilde{\theta}_{ab}$ and \tilde{q}_{ab} are the local displacement, traction, temperature and flux density coefficients associated with the control point with indices a and b . When control points are shared between adjacent elements, physical quantities $\tilde{\mathbf{u}}_{ab}$, $\tilde{\mathbf{t}}_{ab}$, $\tilde{\theta}_{ab}$ and \tilde{q}_{ab} will apply to all isogeometric elements to which the control point with indices a, b belongs, providing a continuous BEM formulation.

Based on these NURBS expansions, the boundary integral equation (11) can be written in a discretized form

$$\begin{aligned} \mathbf{C}(\mathbf{s}_c) \sum_{a_0=1}^{p+1} \sum_{b_0=1}^{q+1} R_{a_0 b_0}^{e_0}(\mathbf{s}_c) \tilde{\mathbf{u}}_{a_0 b_0}^{e_0} + \sum_{e=1}^{N_e} \sum_{a=1}^{p+1} \sum_{b=1}^{q+1} \mathbb{T}_{ab}^e(\mathbf{s}_c, \mathbf{s}_e) \tilde{\mathbf{u}}_{ab}^e = \sum_{e=1}^{N_e} \sum_{a=1}^{p+1} \sum_{b=1}^{q+1} \mathbb{U}_{ab}^e(\mathbf{s}_c, \mathbf{s}_e) \tilde{\mathbf{t}}_{ab}^e \\ + \sum_{e=1}^{N_e} \sum_{a=1}^{p+1} \sum_{b=1}^{q+1} \mathbb{M}_{ab}^e(\mathbf{s}_c, \mathbf{s}_e) \tilde{\theta}_{ab}^e + \sum_{e=1}^{N_e} \sum_{a=1}^{p+1} \sum_{b=1}^{q+1} \mathbb{N}_{ab}^e(\mathbf{s}_c, \mathbf{s}_e) \tilde{q}_{ab}^e \end{aligned} \quad (25)$$

where

$$\mathbb{T}_{ab}^e(\mathbf{s}_c, \mathbf{s}_e) = \int_{-1}^1 \int_{-1}^1 \mathbf{T}(\mathbf{s}_c, \mathbf{s}_e) R_{ab}^e(\mathbf{s}_e) J_e(\mathbf{s}_e) d\tilde{\xi}_e d\tilde{\eta}_e \quad (26)$$

$$\mathbb{U}_{ab}^e(\mathbf{s}_c, \mathbf{s}_e) = \int_{-1}^1 \int_{-1}^1 \mathbf{U}(\mathbf{s}_c, \mathbf{s}_e) R_{ab}^e(\mathbf{s}_e) J_e(\mathbf{s}_e) d\tilde{\xi}_e d\tilde{\eta}_e \quad (27)$$

$$\mathbb{M}_{ab}^e(\mathbf{s}_c, \mathbf{s}_e) = \int_{-1}^1 \int_{-1}^1 \mathbf{M}(\mathbf{s}_c, \mathbf{s}_e) R_{ab}^e(\mathbf{s}_e) J_e(\mathbf{s}_e) d\tilde{\xi}_e d\tilde{\eta}_e \quad (28)$$

$$\mathbb{N}_{ab}^e(\mathbf{s}_c, \mathbf{s}_e) = \int_{-1}^1 \int_{-1}^1 \mathbf{N}(\mathbf{s}_c, \mathbf{s}_e) R_{ab}^e(\mathbf{s}_e) J_e(\mathbf{s}_e) d\tilde{\xi}_e d\tilde{\eta}_e \quad (29)$$

c indicates the collocation point index, $\mathbf{s}_c = (\tilde{\xi}_c, \tilde{\eta}_c)$ the parametric coordinate of the collocation point, e_0 the element in which the collocation point is located, and a_0, b_0 are the local indices of the collocation point in element e_0 . e indicates the element index, $\mathbf{s}_e = (\tilde{\xi}_e, \tilde{\eta}_e)$ the parametric coordinate of the field point in its parent element with $(\tilde{\xi}_e, \tilde{\eta}_e) \in [-1, 1] \times [-1, 1]$, and a, b are local indices of a basis function (or control point) in element e . \mathbf{U} and \mathbf{T} denote the displacement and traction fundamental solution kernels shown in Eqs. (8) and (9), respectively; kernels \mathbf{M} and \mathbf{N} are given in Eqs. (12) and (13). R_{ab}^e denotes the local basis function in element e , and J_e is the Jacobian of transformation from the isogeometric element Γ_e (with knot span $[\xi_i, \xi_{i+1}] \times [\eta_j, \eta_{j+1}]$) to the parent element, this Jacobian being obtained using [72, 73]

$$J_e(\mathbf{s}_e) = |\mathbf{J}_{\xi_e, \eta_e}^e| \cdot |\mathbf{J}_{\xi_e, \tilde{\eta}_e}^e| \quad (30)$$

where $\mathbf{J}_{\xi_e, \eta_e}^e$ is the Jacobian matrix of the geometry mapping defined in Eq. (17), its determinant $|\mathbf{J}_{\xi_e, \eta_e}^e|$, being given by

$$|\mathbf{J}_{\xi_e, \eta_e}^e| = \left| \left(\frac{\partial x_1}{\partial \xi_e}, \frac{\partial x_2}{\partial \xi_e}, \frac{\partial x_3}{\partial \xi_e} \right) \times \left(\frac{\partial x_1}{\partial \eta_e}, \frac{\partial x_2}{\partial \eta_e}, \frac{\partial x_3}{\partial \eta_e} \right) \right| \quad (31)$$

The determinant $|\mathbf{J}_{\xi_e, \tilde{\eta}_e}^e|$ of the Jacobian transformation from the parent domain to parametric domain may be calculated as

$$|\mathbf{J}_{\xi_e, \tilde{\eta}_e}^e| = \frac{1}{4} (\xi_{i+1} - \xi_i) (\eta_{j+1} - \eta_j) \quad (32)$$

If the discretized BIE in Eq. (26) is applied consecutively for all the collocation points located at the points on Γ corresponding to the Greville abscissae [74] of the knot vectors, a system of linear algebraic

equations for IGABEM can be obtained. Application of the boundary conditions then yields the final form of the linear system through which the unknown displacement, traction, temperature and flux density coefficients can be obtained.

In this work, multizone BEM [64, 72] is adopted to deal with models containing two or more materials (such as a substrate and coating). For a substrate with coatings, control points on the interface (between the substrate and coating) do not have known displacement, traction, temperature and flux density coefficients. Instead, we must impose: (i) continuity of displacements and temperatures on the interface; (ii) equilibrium conditions.

The main novel contribution of this paper is the development of new schemes for the evaluation of near-singular integrals. The weakly singular and strongly singular integrals will be computed by the power series expansion method [75, 76]. Since the thickness of TBCs is typically 1 to 5 μm [1], the implementation of 3D IGABEM for such structures is complicated by the distance r (contained in the fundamental solutions Eqs. (8) and (9)) becoming very small, which will lead to a challenging near-singularity in the boundary integrals (26)-(29). Based on the 2D scheme presented in [2], we present a novel 3D scheme capable of producing accurate and efficient solutions for such cases.

3. Accuracy and efficiency of methods of evaluating nearly singular integrals on isogeometric elements

3.1. Adaptive integral method on a surface isogeometric element

A classical 2D Gaussian quadrature formula can be expressed as [49]

$$I = \int_{-1}^1 \int_{-1}^1 F(\tilde{\xi}, \tilde{\eta}) d\tilde{\xi} d\tilde{\eta} = \sum_{i=1}^{m_1} \sum_{j=1}^{m_2} w_1^i w_2^j F(\tilde{\xi}^i, \tilde{\eta}^j) + E_1 + E_2. \quad (33)$$

where $\tilde{\xi}^i, \tilde{\eta}^j$ are the Gauss coordinates, w_1^i, w_2^j the weights, m_1, m_2 Gauss orders, and E_1, E_2 are integration errors corresponding to the two directions. When this is used for BEM integrals, Mustoe [77] showed that the upper bound of relative error E_i/I in the i th direction may be expressed using

$$\frac{E_i}{I} \leq 2 \left(\frac{L_i}{4d} \right)^{2m_i} \frac{(2m_i + \beta - 1)!}{(2m_i)!(\beta - 1)!} \quad (34)$$

where β is the order of singularity (i.e. the integrand behaves like $r^{-\beta}$), d is the minimum distance from the source point to the element, and L_i is the length of the curve in the i th direction through the element center $(\xi_0, \eta_0) = (\frac{\xi_{i+1} + \xi_i}{2}, \frac{\eta_{j+1} + \eta_j}{2})$. For an isogeometric surface element Γ_e (contained in the knot span $[\xi_i, \xi_{i+1}] \times [\eta_j, \eta_{j+1}]$), the lengths L_1 and L_2 can be evaluated simply by using

$$L_1 = \int_{\xi_i}^{\xi_{i+1}} |\mathbf{J}_{\xi_e, \eta_e}^e(\xi, \eta_0)| d\xi = \int_{\xi_i}^{\xi_{i+1}} \sqrt{\sum_{l=1}^{p+1} \left(\frac{\partial x_l}{\partial \xi} \right)^2} d\xi \quad (35)$$

and

$$L_2 = \int_{\eta_j}^{\eta_{j+1}} |\mathbf{J}_{\xi_e, \eta_e}^e(\xi_0, \eta)| d\eta = \int_{\eta_j}^{\eta_{j+1}} \sqrt{\sum_{l=1}^{q+1} \left(\frac{\partial x_l}{\partial \eta} \right)^2} d\eta, \quad (36)$$

respectively.

According to [50, 78], the number of Gauss points required to keep the integration error below a target error \bar{e}_i can be determined from the relationship

$$m_i = \sqrt{\frac{2}{3}\beta + \frac{2}{5}} \left[-\frac{1}{10} \ln\left(\frac{\bar{e}_i}{2}\right) \right] \left[\left(\frac{8L_i}{3d} \right)^{3/4} + 1 \right] \quad (37)$$

which can be further rearranged to yield

$$L_i = \frac{3}{8}d \left(\frac{-10m_i}{\sqrt{2\beta/3 + 2/5 \ln(\bar{e}_i/2)}} - 1 \right)^{4/3} \quad (38)$$

150 The adaptive integration method is based on the above formulae in conjunction with an element sub-
 division algorithm [49]. A full discussion of the method is beyond this paper, but a good introduction for
 conventional BEM can be found in [50] and its implementation in IGABEM in [2, 79, 80]. The key idea
 is the reduction of the ratios $\frac{L_i}{d}$ by progressive subdivision of the element. However, to achieve acceptable
 155 results for large number of near-singular integrals arising in the analysis of 3D coatings or thin sections, the
 number of subdivisions can grow excessively and the computing time will increase dramatically, rendering
 the method prohibitively inefficient for 3D IGABEM analysis of this type of problem.

3.2. Sinh transformation method on a surface isogeometric element

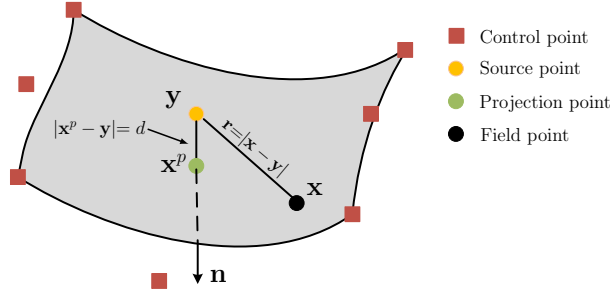


Figure 2: Minimum distance d to the element when $\mathbf{x}^p \in \Gamma_e$

Consider a general isogeometric surface element Γ_e described by the knot span $[\xi_i, \xi_{i+1}) \times [\eta_j, \eta_{j+1})$ as shown in Fig. 2. Similar to the curve case in [2], the minimum distance d from the source point \mathbf{y} to the surface is defined as $|\mathbf{x}^p - \mathbf{y}|$, where $\mathbf{x}^p(\xi_p, \eta_p)$ is the projection point of \mathbf{y} onto the integration element Γ_e and ξ_p, η_p (with $\xi_i \leq \xi_p \leq \xi_{i+1}$ and $\eta_j \leq \eta_p \leq \eta_{j+1}$) are the local intrinsic coordinates of \mathbf{x}^p , i.e.

$$\mathbf{x}^p(\xi_p, \eta_p) = (x_1(\xi_p, \eta_p), x_2(\xi_p, \eta_p), x_3(\xi_p, \eta_p)) = \sum_{a=1}^{p+1} \sum_{b=1}^{q+1} R_{ab}(\xi_p, \eta_p) \mathbf{P}_{ab}^k \quad (39)$$

where \mathbf{P}_{ab}^k is the k ($k = 1, 2, 3$) coordinate of the control point with indices a and b for the considered element.

As shown in Fig. 2, the minimum distance d is the perpendicular distance from the source point \mathbf{y} (which could be a collocation point or internal point) to the projection point \mathbf{x}^p , and the following relation holds

$$x_k^p - y_k = d \cdot n_k(\xi_p, \eta_p) \quad (40)$$

160 where $k = 1, 2, 3$ and $n_k(\xi_p, \eta_p)$ is the component of the unit outward normal \mathbf{n} of the surface at \mathbf{x}^p . The values of distance d and local intrinsic coordinates ξ_p and η_p can be obtained by a Newton-Raphson iterative scheme as presented in [49], and more details for IGABEM implementations can be found in [79, 80].

From Eq. (17), the field point $\mathbf{x} \in \Gamma_e$ can be expressed in terms of a rational polynomial with respect to ξ and η . After using the Taylor expansion of $\mathbf{x}(\xi, \eta)$ around the projection point $\mathbf{x}^p(\xi_p, \eta_p)$ in the parameter

165 space, the expression $x_k - y_k$ can be written as:

$$\begin{aligned} x_k - y_k &= x_k - x_k^p + x_k^p - y_k \\ &= d \cdot n_k + \left(g \frac{\partial}{\partial \xi} + h \frac{\partial}{\partial \eta} \right) x_k(\xi_p, \eta_p) + \frac{1}{2} \left(g \frac{\partial}{\partial \xi} + h \frac{\partial}{\partial \eta} \right)^2 x_k(\xi_p, \eta_p) + \cdots \\ &+ \frac{1}{n!} \left(g \frac{\partial}{\partial \xi} + h \frac{\partial}{\partial \eta} \right)^n x_k(\xi_p, \eta_p) + \text{HOT} \end{aligned} \quad (41)$$

where $k = 1, 2, 3$, $\mathbf{x} = (x_1, x_2, x_3)$, $\mathbf{y} = (y_1, y_2, y_3)$, $\mathbf{x}^p = (x_1^p, x_2^p, x_3^p)$, $g = \xi - \xi_p$, $h = \eta - \eta_p$,

$$\left(g \frac{\partial}{\partial \xi} + h \frac{\partial}{\partial \eta} \right)^n x_k(\xi_p, \eta_p) = \sum_{l=0}^n C_n^l \frac{\partial^n}{\partial \xi^l \partial \eta^{n-l}} x_k(\xi_p, \eta_p) g^l h^{n-l} \quad (42)$$

n is the order of Taylor expansion and HOT abbreviates Higher Order Terms. The partial derivatives in the above equation can be obtained by

$$\frac{\partial^n}{\partial \xi^l \partial \eta^{n-l}} x_k(\xi, \eta) = \sum_{a=1}^{p+1} \sum_{b=1}^{q+1} \frac{\partial^n}{\partial \xi^l \partial \eta^{n-l}} R_{ab}(\xi, \eta) \mathbf{P}_{ab}^k \quad (43)$$

The high-order derivatives of NURBS are given by [70]

$$\begin{aligned} R_{ab}^{(l,m)} &= \frac{1}{W^{(0,0)}} \left(A_{ab}^{(l,m)} - \sum_{i=1}^l \binom{l}{i} W^{(i,0)} R_{ab}^{(l-i,m)} - \sum_{j=1}^m \binom{m}{j} W^{(0,j)} R_{ab}^{(l,m-j)} \right. \\ &\quad \left. - \sum_{i=1}^l \binom{l}{i} \sum_{j=1}^m \binom{m}{j} W^{(i,j)} R_{ab}^{(l-i,m-j)} \right) \end{aligned} \quad (44)$$

where

$$\binom{l}{i} = \frac{l!}{i!(l-i)!}, \quad (45)$$

$$A_{ab}^{(l,m)} = \frac{d^l N_{a,p}(\xi)}{d\xi^l} \frac{d^m N_{b,q}(\eta)}{d\eta^m}, \quad (46)$$

and

$$W^{(i,j)} = \frac{d^{i+j} W(\xi, \eta)}{d\xi^i d\eta^j} = \sum_{a=1}^{p+1} \sum_{b=1}^{q+1} \frac{d^i N_{a,p}(\xi)}{d\xi^i} \frac{d^j N_{b,q}(\eta)}{d\eta^j} w_{ab} \quad (47)$$

Introducing the term

$$D_k^n = \frac{1}{2} \left(g \frac{\partial}{\partial \xi} + h \frac{\partial}{\partial \eta} \right)^2 x_k(\xi_p, \eta_p) + \cdots + \frac{1}{n!} \left(g \frac{\partial}{\partial \xi} + h \frac{\partial}{\partial \eta} \right)^n x_k(\xi_p, \eta_p) \quad (48)$$

where n is the order of the Taylor expansion in Eq. (41), allows (41) to be compactly rewritten as

$$x_k - y_k = d \cdot n_k + h \frac{\partial x_k}{\partial \xi} + g \frac{\partial x_k}{\partial \eta} + D_k^n + \text{HOT} \quad (49)$$

Further, the geometric relationship between the unit outward normal \mathbf{n} and the tangential plane at \mathbf{x}^p , implies

$$n_k \cdot \frac{\partial x_k}{\partial \xi} = n_k \cdot \frac{\partial x_k}{\partial \eta} = 0 \quad (50)$$

By means of Eqs. (49) and (50), r^2 can be expressed as

$$\begin{aligned} r^2(\xi, \eta) &= (x_k - y_k)(x_k - y_k) \\ &= d^2 + \left((\xi - \xi_p) \frac{\partial x_k}{\partial \xi} + (\eta - \eta_p) \frac{\partial x_k}{\partial \eta} \right) \left((\xi - \xi_p) \frac{\partial x_k}{\partial \xi} + (\eta - \eta_p) \frac{\partial x_k}{\partial \eta} \right) \\ &\quad + 2 \left(d \cdot n_k + (\xi - \xi_p) \frac{\partial x_k}{\partial \xi} + (\eta - \eta_p) \frac{\partial x_k}{\partial \eta} \right) D_k^n + D_k^n D_k^n + E_{\text{trun}} \end{aligned} \quad (51)$$

where the summation rule is applied with respect to the index $k = 1, 2, 3$ and E_{trun} is the truncation error arising from neglecting the higher order terms in the Taylor expansion (49).

As is well known in BEM, a near-singularity arises when the point \mathbf{y} is very close to the boundary; this occurs frequently in the analysis of thin sections and coatings. Let us consider the following near-singular boundary integral I^e on a surface isogeometric element Γ_e contained in knot span $[\xi_i, \xi_{i+1}] \times [\eta_j, \eta_{j+1}]$:

$$I^e = \int_{\Gamma_e} \frac{\bar{f}(\mathbf{y}, \mathbf{x})}{r^\beta} d\Gamma(\mathbf{x}) \quad (52)$$

Here, β is a real constant, and \bar{f} is a well-behaved function.

In order to simplify the kernels, the taking of a square root in the computation of distance r (in Eq. (10)) is avoided by writing (52) in terms of r^2 , i.e.

$$I^e = \int_{\Gamma_e} \frac{f(\mathbf{y}, \mathbf{x})}{(r^2)^\beta} d\Gamma(\mathbf{x}) \quad (53)$$

170 where $f(\mathbf{y}, \mathbf{x}) = r^\beta \bar{f}(\mathbf{y}, \mathbf{x})$.

The knot span will be split into four sub-knot spans $[\xi_i, \xi_p] \times [\eta_j, \eta_p]$, $[\xi_p, \xi_{i+1}] \times [\eta_j, \eta_p]$, $[\xi_i, \xi_p] \times [\eta_p, \eta_{j+1}]$ and $[\xi_p, \xi_{i+1}] \times [\eta_p, \eta_{j+1}]$ at the projection point \mathbf{x}^p , so that $I^e = I_1^e + I_2^e + I_3^e + I_4^e$, where

$$I_1^e = \int_{\xi_i}^{\xi_p} \int_{\eta_j}^{\eta_p} \frac{f(\xi, \eta)}{(r^2)^\beta} d\xi d\eta \quad (54)$$

$$I_2^e = \int_{\xi_p}^{\xi_{i+1}} \int_{\eta_j}^{\eta_p} \frac{f(\xi, \eta)}{(r^2)^\beta} d\xi d\eta \quad (55)$$

$$I_3^e = \int_{\xi_i}^{\xi_p} \int_{\eta_p}^{\eta_{j+1}} \frac{f(\xi, \eta)}{(r^2)^\beta} d\xi d\eta \quad (56)$$

$$I_4^e = \int_{\xi_p}^{\xi_{i+1}} \int_{\eta_p}^{\eta_{j+1}} \frac{f(\xi, \eta)}{(r^2)^\beta} d\xi d\eta \quad (57)$$

To deal with the near-singularity in the integral I_1^e , a 2D nonlinear coordinate transformation mapping $(s, t) \in [-1, 1] \times [-1, 1]$ to the parametric coordinate $(\xi, \eta) \in [\xi_i, \xi_p] \times [\eta_j, \eta_p]$ may be defined as

$$\xi = \xi_p + d \cdot \sinh[a(s - 1)] \quad (58)$$

$$\eta = \eta_p + d \cdot \sinh[b(t - 1)] \quad (59)$$

where

$$a = \frac{1}{2} \operatorname{arcsinh} \left(\frac{\xi_p - \xi_i}{d} \right) \quad (60)$$

$$b = \frac{1}{2} \operatorname{arcsinh} \left(\frac{\eta_p - \eta_j}{d} \right) \quad (61)$$

The Jacobian of this transformation becomes

$$J = d \cdot a \cdot b \cdot \cosh[a(s-1)]\cosh[b(t-1)] \quad (62)$$

Applying the transformation in Eqs. (58) and (59), the squared distance r^2 can be expressed as

$$r^2 = d^2 [1 + F_k(s, t)F_k(s, t) + 2F_k(s, t)G_k^n(s, t) + G_k^n(s, t)G_k^n(s, t)] + E_{\text{trun}} \quad (63)$$

with $F_k(s, t) = \left(\sinh[a(s-1)] \frac{\partial x_k}{\partial \xi} + \sinh[b(t-1)] \frac{\partial x_k}{\partial \eta} \right)$ and $G_k^n(s, t) = D_k^n(s, t)/d$.

Substituting (58), (59) and (63) into (54), I_1^e becomes

$$I_1^e = \frac{1}{d^{2\beta}} \int_{-1}^1 \int_{-1}^1 \frac{d \cdot a \cdot b \cdot \cosh[a(s-1)]\cosh[b(t-1)]f(s, t)}{(1 + F_k(s, t)F_k(s, t) + 2F_k(s, t)G_k^n(s, t) + G_k^n(s, t)G_k^n(s, t))^\beta} ds dt \quad (64)$$

Through the above procedure, the denominator has been transformed into an expression that is guaranteed to exceed 1.0, so the integral I_1^e (shown in (64)) has been fully regularized and can be evaluated directly using Gauss-Legendre quadrature. The evaluation of the remaining integrals I_2^e , I_3^e and I_4^e requires different values a and b , expressions for which are given in Table 1, and the expressions corresponding to (64) become

$$I_2^e = \frac{1}{d^{2\beta}} \int_{-1}^1 \int_{-1}^1 \frac{d \cdot a \cdot b \cdot \cosh[a(s-1)]\cosh[b(t-1)]f(s, t)}{(1 + F_k(s, t)F_k(s, t) + 2F_k(s, t)G_k^n(s, t) + G_k^n(s, t)G_k^n(s, t))^\beta} ds dt \quad (65)$$

$$I_3^e = \frac{1}{d^{2\beta}} \int_{-1}^1 \int_{-1}^1 \frac{d \cdot a \cdot b \cdot \cosh[a(s-1)]\cosh[b(t-1)]f(s, t)}{(1 + F_k(s, t)F_k(s, t) + 2F_k(s, t)G_k^n(s, t) + G_k^n(s, t)G_k^n(s, t))^\beta} ds dt \quad (66)$$

$$I_4^e = \frac{1}{d^{2\beta}} \int_{-1}^1 \int_{-1}^1 \frac{d \cdot a \cdot b \cdot \cosh[a(s-1)]\cosh[b(t-1)]f(s, t)}{(1 + F_k(s, t)F_k(s, t) + 2F_k(s, t)G_k^n(s, t) + G_k^n(s, t)G_k^n(s, t))^\beta} ds dt \quad (67)$$

Table 1: The parameters a and b in the sinh transformation

sub-element	a	b	parameter space (ξ, η)	parameter space (s, t)
1	$\frac{1}{2}\text{arcsinh}(\frac{\xi_p - \xi_i}{d})$	$\frac{1}{2}\text{arcsinh}(\frac{\eta_p - \eta_j}{d})$	$[\xi_i, \xi_p] \times [\eta_j, \eta_p]$	$[-1, 1] \times [-1, 1]$
2	$\frac{1}{2}\text{arcsinh}(\frac{\xi_p - \xi_{i+1}}{d})$	$\frac{1}{2}\text{arcsinh}(\frac{\eta_p - \eta_j}{d})$	$[\xi_p, \xi_{i+1}] \times [\eta_j, \eta_p]$	$[1, -1] \times [-1, 1]$
3	$\frac{1}{2}\text{arcsinh}(\frac{\xi_p - \xi_i}{d})$	$\frac{1}{2}\text{arcsinh}(\frac{\eta_p - \eta_{j+1}}{d})$	$[\xi_i, \xi_p] \times [\eta_p, \eta_{j+1}]$	$[-1, 1] \times [1, -1]$
4	$\frac{1}{2}\text{arcsinh}(\frac{\xi_p - \xi_{i+1}}{d})$	$\frac{1}{2}\text{arcsinh}(\frac{\eta_p - \eta_{j+1}}{d})$	$[\xi_p, \xi_{i+1}] \times [\eta_p, \eta_{j+1}]$	$[1, -1] \times [1, -1]$

3.3. Error analysis

3.3.1. Isogeometric cylindrical surface element

This section is devoted to an error analysis of several existing methods for the evaluation of near-singular integrals over an isogeometric element. The element takes the form of a cylindrical surface subtending a 90° arc, with $R = 1, l = 2$, as shown in Figs. 3a and 3b. The quadratic bivariate NURBS surface definition is based on knot vectors $\Xi = \{0, 0, 0, 1, 1, 1\}$ and $\mathcal{H} = \{0, 0, 0, 1, 1, 1\}$. The control point locations and weights are listed in Table 2. Reference solutions for integrals considered in this section are found numerically using the Matlab function ‘*int(int(I, v₁, a₁, b₁), v₂, a₂, b₂)*’ to convergence, where I is an integral with respect to v_1 (from a_1 to b_1) and v_2 (from a_2 to b_2).

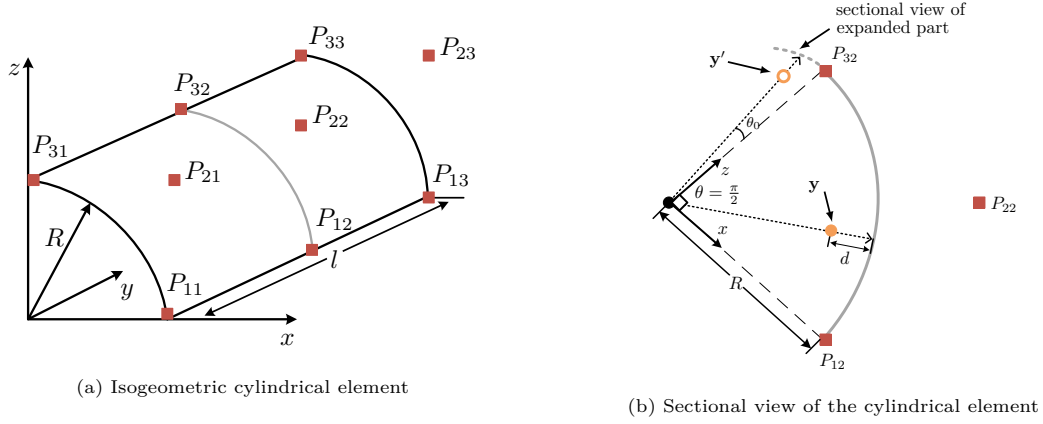


Figure 3: Considered isogeometric cylindrical surface element

Table 2: Control points and weights of the isogeometric cylindrical surface element

Control points	(x, y, z)	weights
1	(1,0,0)	1.0
2	(1,1,0)	1.0
3	(1,2,0)	1.0
4	(1,0,1)	$\sqrt{2}/2$
5	(1,1,1)	$\sqrt{2}/2$
6	(1,2,1)	$\sqrt{2}/2$
7	(0,0,1)	1.0
8	(0,1,1)	1.0
9	(0,2,1)	1.0

The coordinate of the source point \mathbf{y} is chosen as $((R-d)\cos(\pi/4), 1.0, (R-d)\sin(\pi/4))$, in which d is the distance from the source point to the boundary (see Fig. 3b). We define a non-dimensional aspect ratio d^* to describe the proximity of the source point to a curve or surface element, as

$$d^* = \frac{d}{\max(L_1, L_2)} \quad (68)$$

where L_1 and L_2 are the element lengths defined in Eqs. (35) and (36). The order of near-singularity of integrals I^e , as seen in Eq. (52), is defined as: (i) $\beta = 0$, I^e will be a regular integral; (ii) $\beta = 1$, I^e will be a weakly near-singular integral, i.e. (27) and (28); (iii) $\beta = 2$, I^e will be a strongly near-singular integral, i.e. (26). The relative error ε_r is used to describe the numerical solution accuracy at a computed point, i.e.

$$\varepsilon_r = \left| \frac{I_{\text{num}} - I_{\text{ref}}}{I_{\text{ref}}} \right| \quad (69)$$

where I_{num} and I_{ref} are, respectively, the numerical and reference results of the integral evaluation at a single point.

In the following, we will choose one of each of two different levels of near-singular integrals (weakly and strongly near-singular integral), and the kernels can be obtained from the fundamental solutions in Eqs. (8) and (9) with $i = j = 1$, i.e.

$$\int_{\Gamma_e} \frac{1}{16\pi\mu(1-\nu)r} [(3-4\nu) + (r_{,1})^2] d\Gamma(\mathbf{x}) \quad (70)$$

and

$$\int_{\Gamma_e} \frac{-1}{8\pi\mu(1-\nu)r^2} \left\{ \frac{\partial r}{\partial \mathbf{n}} [(1-2\nu) + 3(r_{,1})^2] \right\} d\Gamma(\mathbf{x}) \quad (71)$$

We take the material properties $\mu = 1$ and $\nu = 0.3$. In this section, the Telles scheme presented in [41], which strictly should be used only for weakly singular cases, is included. We acknowledge this scheme will fail for fully singular integrals containing strongly singular kernels, but the aim is to test whether the transformation might be helpful for higher order singularities when dealing with a near-singular integral. Actually, the Telles method used here had been updated by Telles and Oliveira in 1994 [81], in which improved near singular behaviour, treated separately, was proposed for $\ln(1/r)$, $1/r$, $1/r^2$ and $1/r^3$.

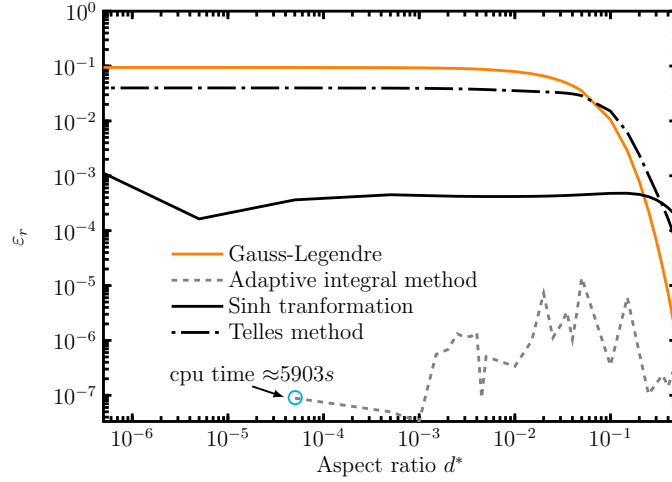


Figure 4: Error analysis for different methods focusing on the weakly near-singular integral

The relative error ε_r in evaluating the weakly near-singular integral in (70) for different methods is presented in Fig. 4. An 8×8 Gauss-Legendre scheme was used for all methods, and the threshold $\bar{\varepsilon} = 10^{-8}$ was taken for the adaptive integral method. When d^* exceeds about 0.4, all the considered methods can provide acceptable results with $\varepsilon_r < 10^{-3}$. However, when $d^* < 0.4$, the Gauss-Legendre and Telles methods become less satisfactory with relative errors ε_r stabilizing at about 10% and 6% respectively. It is noted that through introducing a third degree polynomial transformation the Telles scheme outperforms standard Gauss-Legendre quadrature, though the results are still unsatisfactory when using 8×8 Gauss points. In addition, with same number of Gauss points the relative error of the sinh transformation method remains below 10^{-3} ($< 1\%$) even when the aspect ratio d^* decreases to 10^{-6} . The relative error of the sinh transformation could be decreased further by using more Gauss points in the computation. The relationships between relative error and the number of Gauss points will be discussed in the following. It should be pointed out that, due to neglecting the truncation error E_{trun} in equation (63), when the computed point is not very close to the boundary the relative error of the sinh transformation method is larger than that of conventional Gaussian quadrature and Telles method. By using the scheme of element subdivision, it is clearly seen that the adaptive integral method can achieve very accurate results with relative errors below 10^{-5} ($< 0.001\%$). However, since the computation time increases rapidly, only the results for cases having $d^* \geq 5 \times 10^{-5}$ are shown in Fig. 4.

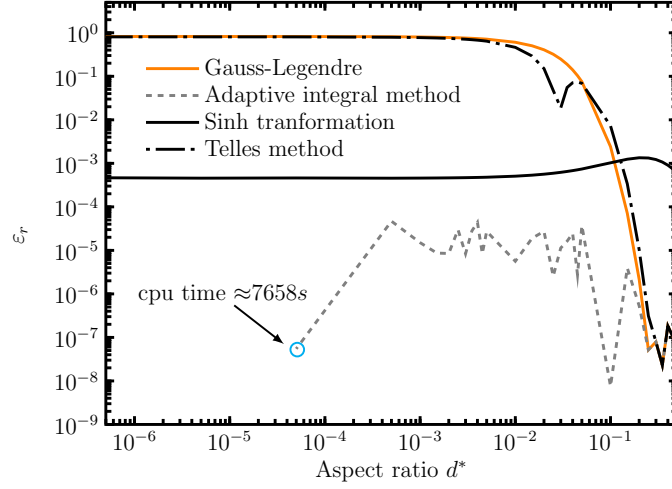


Figure 5: Error analysis for different methods focusing on the strongly near-singular integral

With the increase of the order of near-singularity, corresponding changes are made to the integration schemes tested. We study here the accuracy for the different methods focusing on the strongly near-singular integral given in Eq. (71). Fig. 5 shows the relative error in the evaluation of this integral as a function of the ratio d^* . With the increase in the order of singularity in the kernel, many more Gauss points are required to produce the required accuracy, and for this case a 20×20 Gauss scheme is adopted. From Fig. 5 it is seen that all the considered methods can produce accurate results when the aspect ratio $d^* > 0.3$. However, when $d^* < 0.3$, the results obtained by the Gauss-Legendre quadrature and Telles methods exhibit large errors. Conversely, the sinh transformation method remains capable of delivering high accuracy results with $\varepsilon_r < 10^{-3}$ even for d^* as low as 10^{-6} (indeed, one might say arbitrarily low d^*). It is also evident that the adaptive integral method is still the most accurate approach, with its relative error ε_r remaining around 10^{-5} and one or two orders of magnitude smaller than ε_r found from the sinh transformation method. As shown in Fig. 5, the CPU time for the strongly near-singular integral when $d^* = 5 \times 10^{-5}$ is about 7658s (about 30% more than that required for the weakly near-singular case), and therefore only the relative errors with $d^* \geq 5 \times 10^{-5}$ are shown.

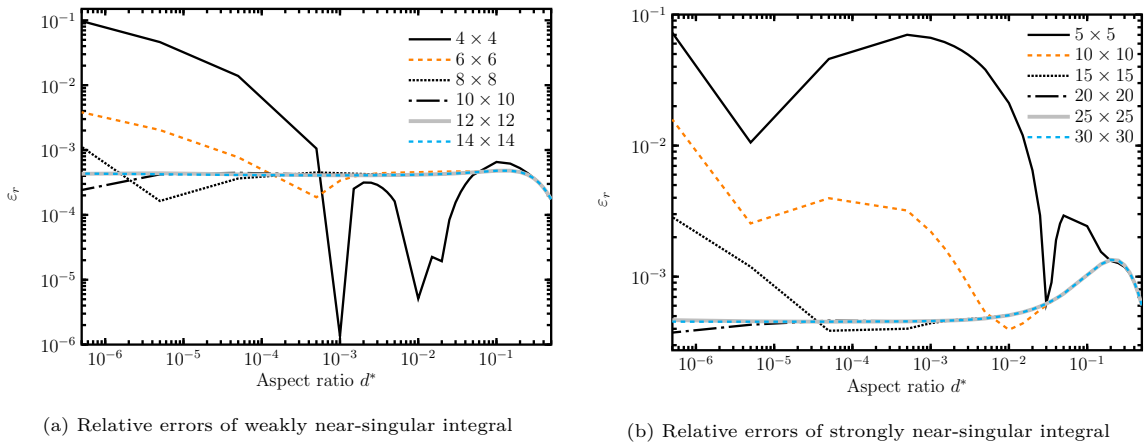


Figure 6: The influence of the number of Gauss points on accuracy of the sinh transformation scheme

The number of Gauss points used in the computation strongly influences the accuracy of the sinh transformation method. This is demonstrated in Figs. 6a and 6b for both weakly and strongly near-singular

integral evaluations. It can be seen from Fig. 6a that the relative errors exhibit marked fluctuations when the number of Gauss points is less than 6×6 . However, with the number of Gauss points increasing to 10×10 , relative errors reach about 4×10^{-4} and remain stable. For the strongly near-singular integral in Fig. 6b, relative errors stabilize at around 5×10^{-4} when the number of Gauss points reaches 25×25 .

From the above accuracy comparisons, we can draw the following conclusions: (i) the adaptive integral method can consistently deliver very high accuracy ($\varepsilon_r < 1.0 \times 10^{-5}$) for both weakly and strongly near-singular integrals, but the computation time can increase with the order of singularity in the kernel; and (ii) the sinh transformation method can achieve satisfactory results ($\varepsilon_r < 1.0 \times 10^{-3}$) with a fixed number of Gauss points in the computation of weakly and strongly near-singular integrals.

3.4. Efficiency analysis for integral method on surface element

In a typical 3D IGABEM analysis of a coated structure, there will be a large number of near-singular integrals that arise, and the development of a scheme to evaluate them efficiently with acceptable accuracy is of great importance.

The error analysis in Section 3.3 suggests that both the adaptive method and the sinh transformation method are promising schemes that can deliver the required accuracy. In this section, the two schemes will be further studied from the perspective of computational efficiency. The weakly near-singular integral in Eq. (70) and strongly near-singular integral in Eq. (71) on the surface element shown in Fig. 3a are considered. Taking our lead from the conclusions of the error analysis, 8×8 and 20×20 Gauss point distributions are used for the computation of integrals containing the weakly singular and strongly singular kernels, respectively, and it is for this reason that the evaluation of the strongly near-singular integral using the sinh transformation takes much more time than that of the weakly near-singular integral in Figs. 7a and 7b. Since a fixed number of Gauss points has been used in the sinh transformation method, the CPU time of the scheme is displayed as a horizontal line. For the adaptive integral method, the CPU time of the scheme with three different error tolerances $\bar{\varepsilon} = 10^{-6}, 10^{-8}$ and 10^{-10} is compared in Figs. 7a and 7b. It should be pointed out that the same error tolerances are used on both integration directions, i.e. $\bar{\varepsilon}_1 = \bar{\varepsilon}_2 = \bar{\varepsilon}$. From Figs. 7a and 7b, the effect of reducing the error tolerance on increasing the run time can clearly be seen. The CPU time and aspect ratio d^* are broadly linearly related for both weakly and strongly near-singular integrals with a fixed error tolerance. An obvious feature of these performance graphs is that there is an intersection where the CPU times for the sinh transformation and adaptive integral methods coincide, suggesting a break-even point.

The total number of sub-elements and Gauss points used in the adaptive method for weakly near-singular integrals is given in Table 3. As shown in the Table, when $d^* = 0.5$, the element subdivision algorithm will not be required. However, when d^* reduces to 0.0005 a large number of sub-elements will be produced, significantly increasing the computation time. We can also observe that each reduction of two orders of magnitude in $\bar{\varepsilon}$ results in an increase of about 26% in the number of sub-elements and Gauss points. The Gauss point distributions over the parametric domain in the adaptive integral method are shown in Figs. 8(a),(b),(c) and (d). When a near-singularity occurs (Figs. 8 (b), (c) and (d)), a very refined grid is produced as the scheme controls the aspect ratio L_i/d .

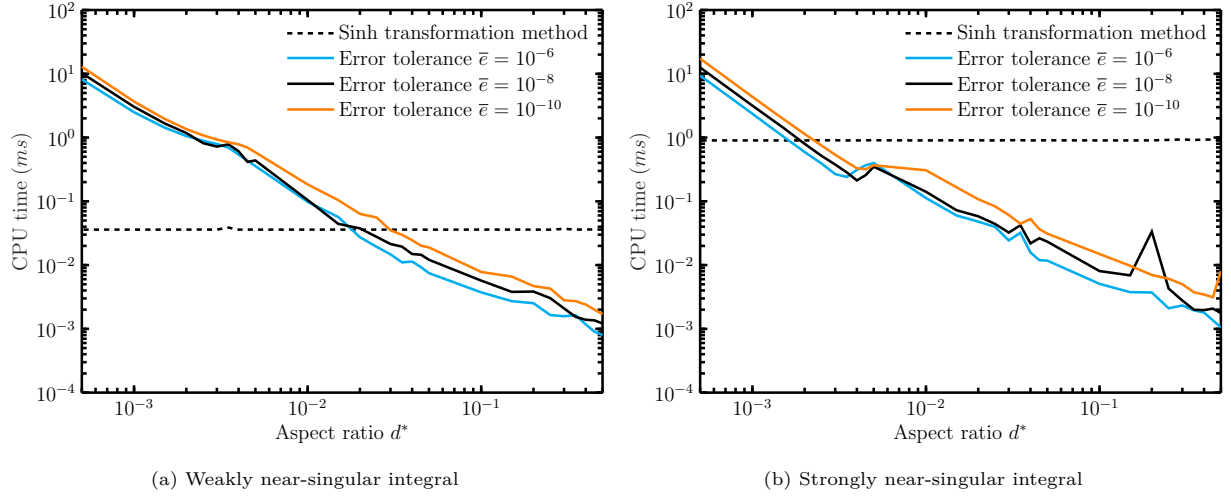


Figure 7: CPU time comparison between adaptive integral method and sinh transformation method on isogeometric cylindrical element

Table 3: Total number of sub-elements and Gauss points used in the adaptive method for weakly near-singular integrals on cylindrical element

Error tolerance $\bar{\epsilon}$	10^{-6}		10^{-8}		10^{-10}	
Aspect ratio d^*	No. SE	No. GP	No. SE	No. GP	No. SE	No. GP
5.0×10^{-1}	1	60	1	112	1	170
3.5×10^{-1}	1	180	2	143	2	229
2.0×10^{-1}	4	210	4	359	6	419
5.0×10^{-2}	40	391	54	873	60	1654
3.5×10^{-2}	77	482	96	1416	126	2149
2.0×10^{-2}	228	1194	294	2147	360	4166
5.0×10^{-3}	3431	13888	4346	18238	5580	26054
3.5×10^{-3}	6968	28054	8892	36502	11220	48522
2.0×10^{-3}	21294	85358	27060	109166	34419	141268
5.0×10^{-4}	340704	1363329	431613	1727300	548262	2196730

Note: ‘No. SE’ stands ‘number of sub-elements’; ‘No. GP’ indicates ‘number of Gauss points’.

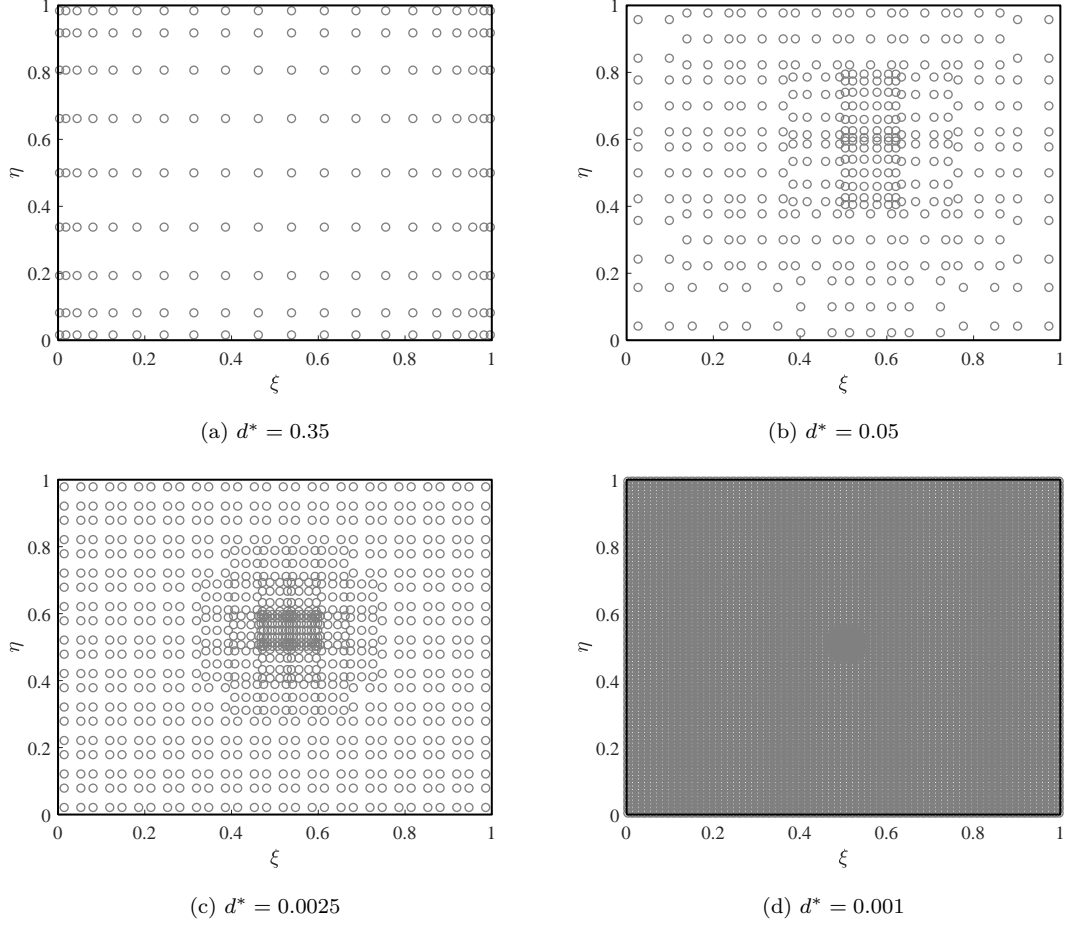


Figure 8: Gauss points distribution in computed domain by adaptive integral method (projection point lies in center of the considered element)

4. Extended sinh transformation on surface element

Depending on the location of the source point or internal point being considered, near-singular integrals can be divided into two types: (i) those for which the projection point lies inside the element (i.e. $\mathbf{x}^p \in \Gamma_e$, shown in Fig. 2), (ii) those for which the projection point lies outside the element (i.e. $\mathbf{x}^p \notin \Gamma_e$; a case is illustrated in Fig. 3b). As discussed in Section 3.2, the conventional sinh transformation method can easily deal with the case when the projection point lies inside the considered element. However, for coatings or thin sections, it will quite commonly occur that a projection point lies outside the element in a near-singular integral. In this section, based on the analytical extension of the NURBS surface, a new adaptation of the sinh transformation for an isogeometric surface element is presented to deal with these cases. To distinguish between projection points inside and outside the knot span, we denote a projection point that is outside the knot span by $\mathbf{x}^{p'}$.

Let us take the biquadratic isogeometric cylindrical surface element shown in Figs. 3a and 3b as an example. Without loss of generality, let the knot span of the isogeometric element be $[0, 1] \times [0, 1]$. For this element, the B-spline basis functions $N_i(\xi)$ and $N_j(\eta)$ for NURBS basis functions $R_{ij}(\xi, \eta)$ can be obtained easily. Since the basis functions $N_i(\xi)$ and $N_j(\eta)$ are a set of continuous functions of $(\xi, \eta) \in \mathbb{R}^2$, they can be evaluated for values of $(\xi, \eta) \notin [0, 1]^2$ to consider points outside the element. Fig. 9 shows the basis functions $N_i(\xi)$ and $N_j(\eta)$ evaluated over the interval $(\xi, \eta) \in [0, 1.2]^2$; the element is shown in white and the

extended domain is shown shaded. In the extended sinh transformation method, when the projection point $(\xi_{p'}, \eta_{p'})$ is located outside of the knot span, the analytical extension of the basis functions in the extended span (shaded region in Fig. 9) will be used. Then the expanded isogeometric element can be expressed by

$$\mathbf{x}(\xi, \eta) = \sum_{a=1}^{p+1} \sum_{b=1}^{q+1} R_{ab}(\xi, \eta) \mathbf{P}_{ab} \quad (72)$$

where $\xi \in [0, \xi_{p'}]$, $\eta \in [0, \eta_{p'}]$. For the cases in which the projection point is just outside the other side of the knot span, a similar expression can be used with $\xi_{p'}, \eta_{p'} < 0$.

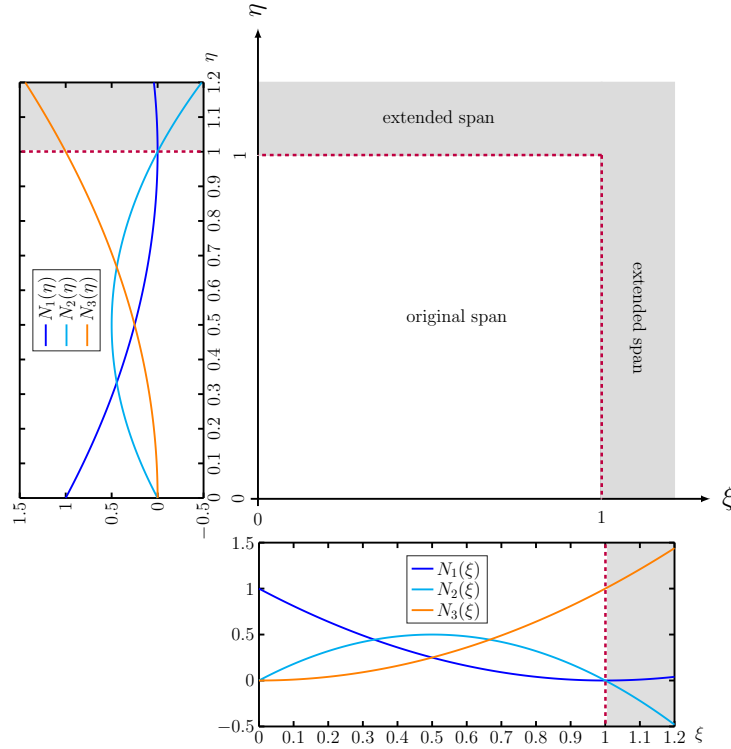


Figure 9: Basis functions of the considered isogeometric element

For the extended isogeometric element, the definition of minimum distance $d = |\mathbf{y} - \mathbf{x}^{p'}|$ will not change but the locations of the projection points move to the analytically extended part of the considered element. Thus, equations (50) and (51) can also be used here, but the expressions for the near-singular integral (53) will be modified. For an isogeometric element with knot span $[\xi_i, \xi_{i+1}] \times [\eta_j, \eta_{j+1}]$, when $\xi_{p'} > \xi_{i+1}$ and $\eta_{p'} > \eta_{j+1}$ (Case 1 in Fig. 10(a)), the integral will become $I^e = I_1^e - I_2^e - I_3^e + I_4^e$, where

$$I_1^e = \int_{\xi_i}^{\xi_{p'}} \int_{\eta_j}^{\eta_{p'}} \frac{f(\xi, \eta)}{(r^2)^\alpha} d\xi d\eta, \quad I_2^e = \int_{\xi_{i+1}}^{\xi_{p'}} \int_{\eta_j}^{\eta_{p'}} \frac{f(\xi, \eta)}{(r^2)^\alpha} d\xi d\eta \quad (73)$$

$$I_3^e = \int_{\xi_i}^{\xi_{p'}} \int_{\eta_{j+1}}^{\eta_{p'}} \frac{f(\xi, \eta)}{(r^2)^\alpha} d\xi d\eta, \quad I_4^e = \int_{\xi_{i+1}}^{\xi_{p'}} \int_{\eta_{j+1}}^{\eta_{p'}} \frac{f(\xi, \eta)}{(r^2)^\alpha} d\xi d\eta \quad (74)$$

For Case 2 with $\xi_{p'} > \xi_{i+1}$ and $\eta_i < \eta_{p'} < \eta_{j+1}$ (in Fig. 10(b)) and Case 3 with $\xi_i < \xi_{p'} < \xi_{i+1}$ and $\xi_{j+1} < \eta_{p'}$ (in Fig. 10(c)), the integral (53) can also be expressed as $I^e = I_1^e - I_2^e - I_3^e + I_4^e$, but with appropriate changes to the limits of integrals I_1^e , I_2^e , I_3^e and I_4^e .

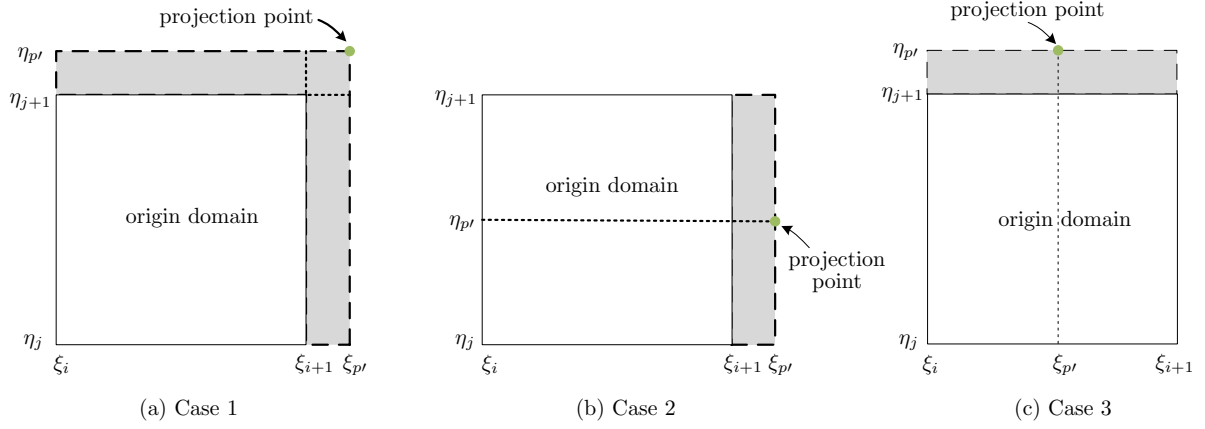


Figure 10: Different locations of projection point in an knot span

5. Implementation of hybrid integration scheme on surface element

From the above discussion it is clear that both the sinh transformation and adaptive approaches have some appealing features for evaluating near-singular integrals in IGABEM, but they also have disadvantages. Since a fixed number of Gauss points is used in the sinh transformation method, the computational efficiency is consistently good, especially for the case where d^* is very small. But neglecting the truncation error E_{trun} will result in some loss of accuracy in numerical computation as the distance from the projection point grows. For the adaptive integral method, the element subdivision means the accuracy of this method is consistently good, but the CPU time requirements present a considerable barrier for its efficient implementation for coatings and other very thin sections. A satisfactory balance between accuracy and efficiency cannot be achieved simultaneously by using only one of the considered methods, but a hybrid scheme is strongly suggested by the fact that the sinh transformation performs well for small d^* and the adaptive scheme performs well for larger d^* . We develop the scheme, named \sinh^+ , in the following section.

5.1. \sinh^+ scheme

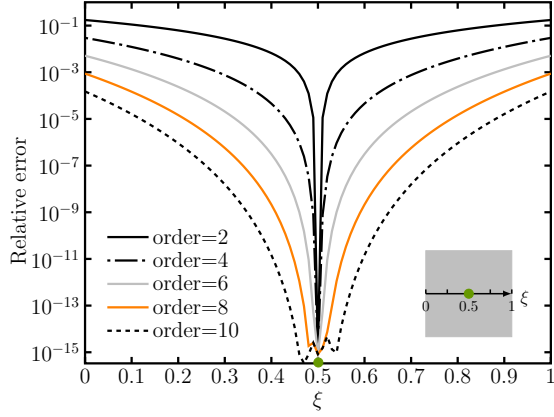
The hybrid \sinh^+ scheme involves integrating some regions of the element using the sinh transformation and other regions with the adaptive method. The element partitioning into these subregions is decided by monitoring of the truncation error term E_{trun} that appears in Eqs. (51) and (63).

From Eq. (63), the term E_{trun} can be written

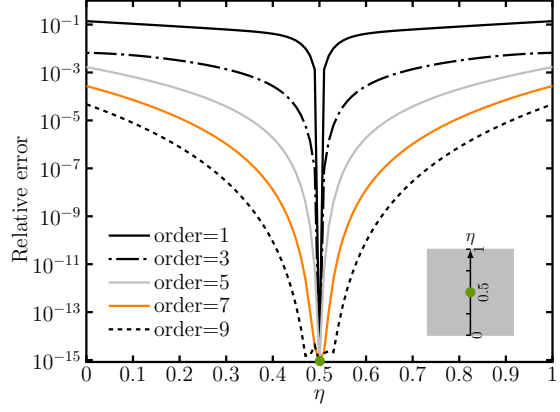
$$E_{\text{trun}} = |r_{\text{exact}}^2 - d^2 [1 + F_k(s, t)F_k(s, t) + 2F_k(s, t)G_k^n(s, t) + G_k^n(s, t)G_k^n(s, t)]| \quad (75)$$

where r_{exact}^2 is the square distance between the source point and field point; this can be easily evaluated since the coordinates of the source point and the field (Gauss) point are known. This provides the possibility of defining a relative error norm Re_{trun} , as follows, to describe the accuracy of predicting the square distance r^2 in Eq. (63).

$$\text{Relative error}(\text{Re}_{\text{trun}}) = \left| \frac{r_{\text{exact}}^2 - d^2 [1 + F_k(s, t)F_k(s, t) + 2F_k(s, t)G_k^n(s, t) + G_k^n(s, t)G_k^n(s, t)]}{r_{\text{exact}}^2} \right| \quad (76)$$

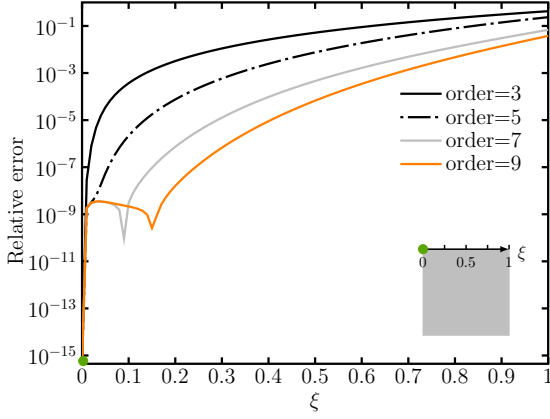


(a) Relative error of predicting r^2 along ξ direction

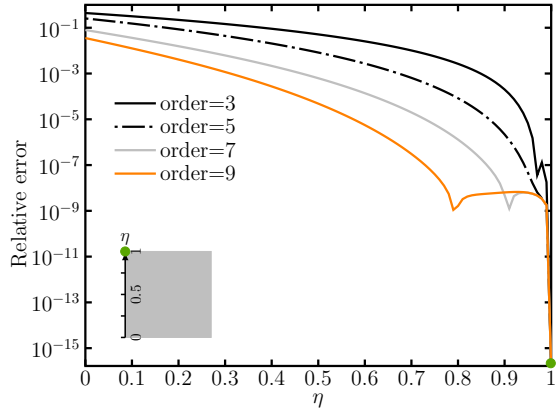


(b) Relative error of predicting r^2 along η direction

Figure 11: Relative error of predicting r^2 when the projection point lies in the center of an element



(a) Relative error of predicting r^2 along ξ direction



(b) Relative error of predicting r^2 along η direction

Figure 12: Relative error of predicting r^2 when the projection point lies in the corner of an element

For a surface element, there are two parameters ξ and η in the Taylor expansion as shown in Eq. (41). In our analysis in the current section, the cylindrical element shown in Fig. 3a will be used to study the relationship between the parametric location ξ, η and the relative error in predicting the square distance r^2 . For the case where the projection point is located at the center of the element ($\xi_p = \eta_p = 0.5$), Figs. 11a and 11b show the relative error (Re_{trun}) comparisons when the Taylor expansion is taken along the ξ and η directions, respectively. From the two figures, we can observe that both the odd and even terms of the Taylor expansion can be obtained with similar relative errors. Figs. 12a and 12b present the relative errors when the projection point lies at a corner ($\xi_p = 0, \eta_p = 1$) of the element, and the relative errors when the projection point lies on the element boundary ($\xi_p = 0.5, \eta_p = 0$) are shown in Figs. 13a and 13b. The growth of the truncation error with increasing distance between the field point and the projection point can be seen clearly. The order referred to in these figures relates to the number of terms (n) used in the Taylor series approximation in Eqs. (41), (51) and (63).

error is below the threshold eps , so the method will be both accurate and computationally efficient in this region. For the remaining region, shown shaded grey in the Figure, the adaptive integral method will be used, and this scheme will be efficient here since the domain of integration is not too close to the projection point. For practical implementation, the (grey) region should be further divided into eight subregions as shown in Fig. 15. It should be noted that both Figs. 14 and 15 show the case when the projection point lies in the center of the element. However, when the projection point lies close to an edge of the element, some of the grey-shaded subdivisions will vanish.

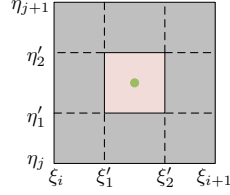


Figure 15: Subdivision scheme for region $[\xi_i, \xi_{i+1}] \times [\eta_j, \eta_{j+1}] - [\xi'_1, \xi'_2] \times [\eta'_1, \eta'_2]$

5.2. Summary of the recommended integration schemes for 3D IGABEM

Since several different integration schemes have been presented, we take the opportunity here to summarize the recommended methods in an implementation of 3D IGABEM:

- Singular integrals: all the singular integrals are computed by the power series expansion method [75, 76].
- Non-singular integrals: These are divided into two categories: regular integrals and near-singular integrals, as defined by the aspect ratio d^* and its relation to a critical value, d^*_{crit} . The critical value may vary in order to allow engineers to achieve a different balance between accuracy and computational efficiency as may be required for different applications. Such a decision might be informed by Figs. 7a and 7b), for example. A larger value will improve computational efficiency by favouring the sinh transformation, while a smaller value will improve accuracy by favouring the adaptive method. In this work, $d^*_{crit} = 0.6$ is adopted for both weakly and strongly near-singular integrals in the numerical examples. This value has been found by numerical testing to provide a reasonable balance between accuracy and efficiency for the problems tested.

(i) If $d^* \geq d^*_{crit}$, the integral will be evaluated by the adaptive integral method. The majority of cases in a typical analysis will be regular and will not require any subdivision. Some near-singular integrals will be computed in this way, i.e. when the central region in Fig. 14 shrinks to zero.

(ii) If $d^* < d^*_{crit}$, the sinh transformation will be used to evaluate the near-singular integral. Here, the element will be subdivided as suggested by the truncation error E_{trun} and truncation error threshold eps . If the projection point is inside the element, the traditional sinh transformation will be used. If the projection point is outside the element, the extended sinh transformation will be adopted.

For the subregion in which $E_{trun} \geq eps$, the adaptive scheme will be used.

For the subregion in which $E_{trun} < eps$, the sinh transformation method will be used.

6. Numerical examples

In order to demonstrate the accuracy and effectiveness of the 3D IGABEM based on the new \sinh^+ scheme, we examine several numerical examples including the evaluation of individual near-singular integrals and the full IGABEM analysis of engineering problems requiring solutions evaluated near the boundary, as well as problems involving coating structures and thin sections. The material properties for thermal barrier

coatings are taken from Padture [1]. The stress-free reference temperature is taken as zero for all cases. Two error metrics are considered: a relative error defined in Eq. (69) and an L^2 relative error norm with respect to a reference solution f_{ref} (here f is any quantity of interest such as displacement, stress, temperature and flux), this norm E_2 being defined by

$$E_2(f_{\text{num}}; \Gamma) = \frac{\|f_{\text{num}} - f_{\text{ref}}\|_{L^2(\Gamma)}}{\|f_{\text{ref}}\|_{L^2(\Gamma)}} \quad (77)$$

where Γ is the surface over which the norm is taken, and f_{num} is the physical quantity (displacement, stress, temperature or flux) as predicted by the numerical scheme. For completeness, we provide a definition of the L^2 norm $\|\cdot\|_{L^2(\Gamma)}$ as

$$\|g\|_{L^2(\Gamma)} = \sqrt{\int_{\Gamma} g^2 d\Gamma} \quad (78)$$

6.1. \sinh^+ scheme over an isogeometric cylindrical surface

To test the proposed \sinh^+ scheme, the weakly and strongly near-singular integrals shown in Eqs. (70) and (71) are evaluated over an isogeometric cylindrical surface element (see Fig. 3a). The control points of the element are given in Table 2. The position of the source point is described by

$$x = (1 - d) \sin(\pi/4), \quad y = 1, \quad z = (1 - d) \cos(\pi/4). \quad (79)$$

Here, we consider d varying from 1 to 0.000001 (the cylinder has unit radius).

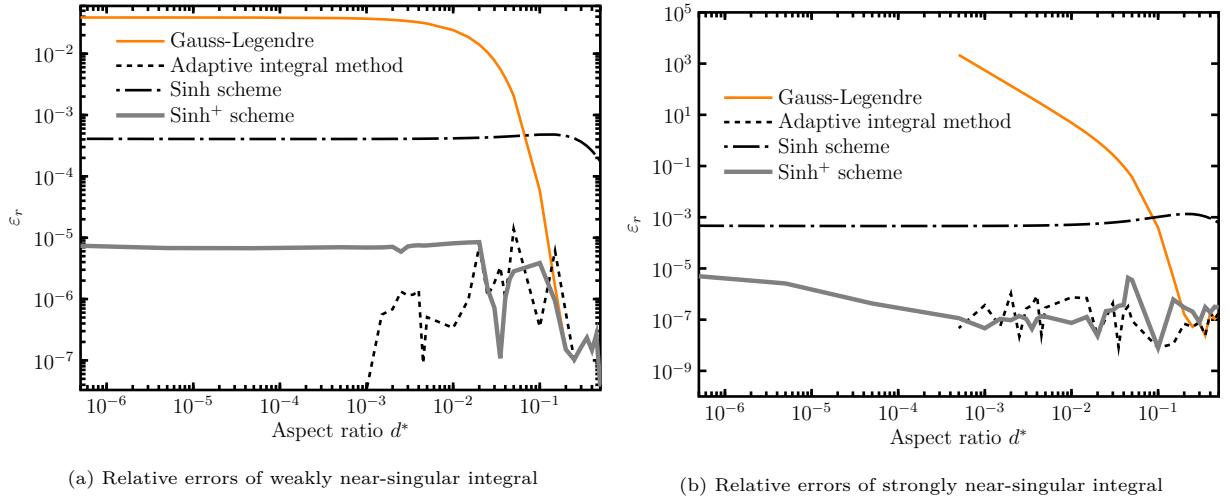


Figure 16: Relative errors comparison among \sinh^+ scheme, \sinh scheme, Gauss-Legendre and adaptive integral method

Figs. 16a and 16b show a comparison of the relative errors produced by the \sinh^+ scheme, \sinh scheme, Gauss-Legendre and adaptive integral method. In the computation, a set of 20×20 Gauss points are used to evaluate the weakly near-singular integral. For the strongly near-singular integral, 25×25 Gauss points are used. An error threshold $\bar{\epsilon} = 10^{-8}$ is taken for the adaptive integral method. It can be clearly seen that the proposed \sinh^+ can produce accurate results with a relative error ϵ_r remaining below 10^{-5} and being one to four orders of magnitude smaller than ϵ_r found with the conventional \sinh transformation methods.

As shown in Fig. 14, the truncation error threshold ϵ_{ps} is a key factor defining the performance of the \sinh^+ scheme. Figs. 17a and 17b show the impact of the choice of ϵ_{ps} on the accuracy of weakly and strongly near-singular integrations. It is noted that by reducing ϵ_{ps} the accuracy of the \sinh^+ scheme will be significantly improved.

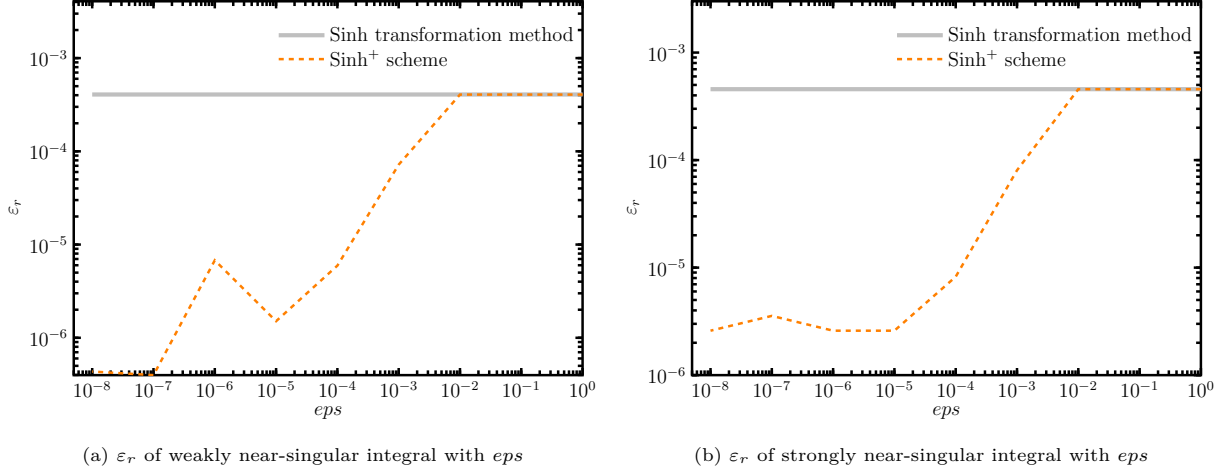


Figure 17: The impact of εps on the accuracy of near-singular integration

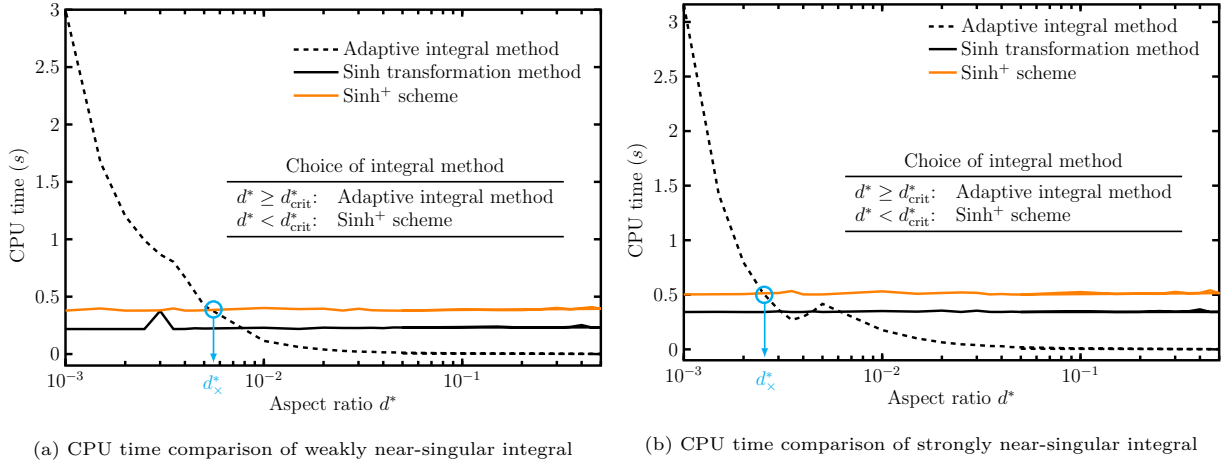


Figure 18: CPU time comparison of near-singular integral evaluations

Figs. 18a and 18b show the CPU time comparison of near-singular integral evaluations with different methods (adaptive integral method, \sinh^+ scheme and the conventional sinh transformation method). When $d^* > d^*_x$, the \sinh^+ scheme can be seen to require a little more time than the adaptive method due to the overhead in computing the parameters ξ'_1, ξ'_2, η'_1 and η'_2 . For $d^* < d^*_x$ the CPU time of the adaptive integral method increases dramatically, while the CPU time of the \sinh^+ scheme remains fixed at around 0.5s.

6.2. Extended \sinh^+ scheme over an isogeometric cylindrical surface

Here, we take the cylindrical element (with knot span $[0, 1] \times [0, 1]$) in Fig. 3a as an example, and consider cases illustrated in Fig. 19, in which the source point is located outside the subtended arc of the element, yet remains close to the element. The position of the source point is described by

$$x = (1 - d) \cos(\theta + \theta_0), y = 1.0, z = (1 - d) \sin(\theta + \theta_0) \quad (80)$$

where $\theta = \pi/2$ and $\theta_0 = \pi/180, \pi/1800, \pi/18000$ are small angles as shown in Fig 19. The distance d varies between 0.9 and 0.000001 (the cylinder has unit radius). Since the projection point lies outside the element, the extended sinh transformation is required. As shown in Fig. 20, the knot span $[\xi_i, \xi_{i+1}] \times [\eta_j, \eta_{j+1}]$ is

divided into two parts. In the pink region $([\xi'_1, \xi'_2] \times [\eta'_1, \eta_p])$, where $\text{Re}_{\text{trun}} < \text{eps}$, the sinh transformation method will be used and the scheme can benefit from its computational efficiency. The adaptive integral method will be used to evaluate the integrals on the remaining grey region where $\text{Re}_{\text{trun}} > \text{eps}$.

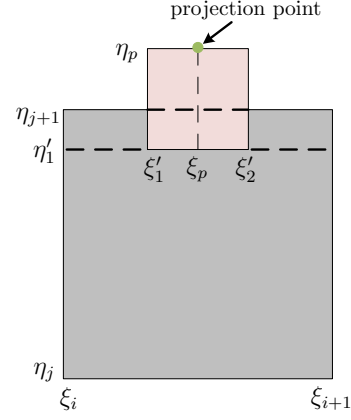
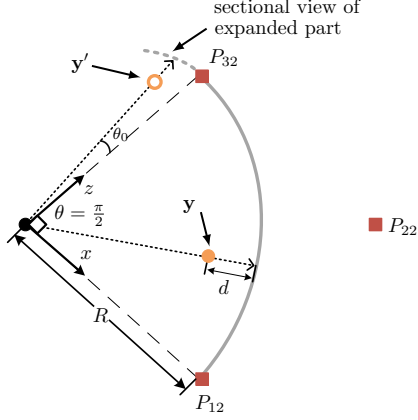


Figure 19: Lateral view of the expanded cylindrical element Figure 20: Subdivision scheme for extended \sinh^+ scheme

Fig. 21 shows the relative errors obtained by the extended sinh transformation for the weakly near-singular integral evaluation over the element. The relative errors ε_r obtained by the extended sinh transformation are very small, generally remaining far below 10^{-5} , even for d^* as low as 10^{-6} .

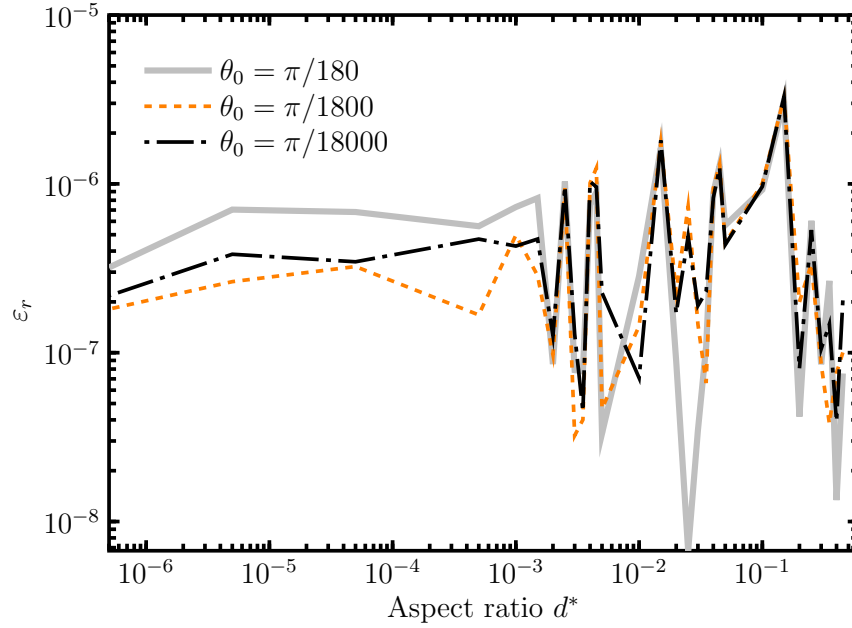


Figure 21: Relative errors obtained by extended sinh transformation for weakly near-singular integral

6.3. Thermoelastic analysis of a cube

In this section we consider the thermal stress analysis of a $2\text{m} \times 2\text{m} \times 2\text{m}$ cube. All six faces of the cube are constrained against displacement in the normal direction (i.e. roller conditions). Young's modulus is taken as $E = 4.0$ GPa, Poisson's ratio as $\nu = 0.34$ and the coefficient of thermal expansion as $\alpha = 1.0 \times 10^{-5}$

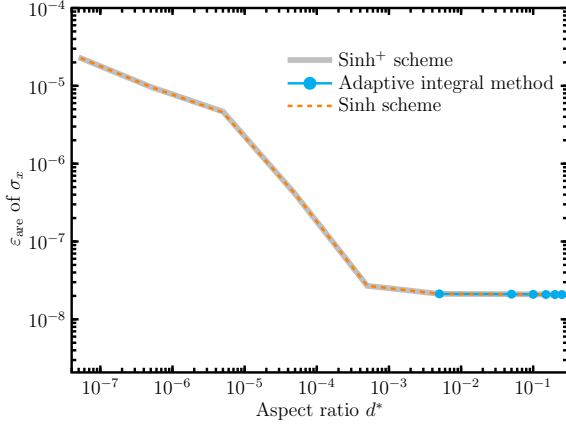


Figure 22: ε_{are} of normal stress σ_x at the internal points

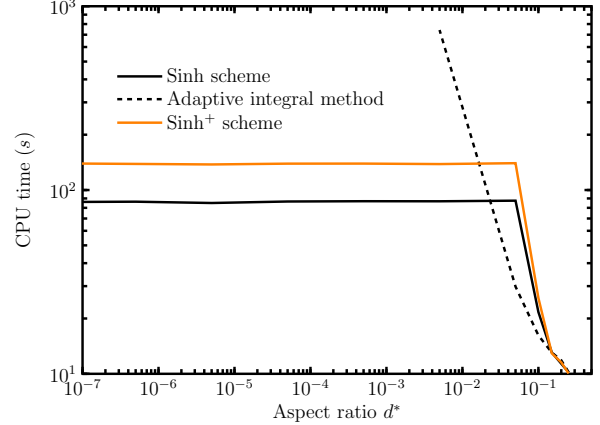


Figure 23: Comparison of CPU time for different methods

$^{\circ}\text{C}^{-1}$. A uniform temperature change $\Delta T = 100^{\circ}\text{C}$ is applied to the cube, and these conditions cause the analytical solution for thermal stresses in the cube to become

$$\sigma_x = \sigma_y = \sigma_z = -\frac{E\alpha\Delta T}{1 - 2\nu} = -12.5 \text{ MPa} \quad (81)$$

In this model, the cube is discretized using only six isogeometric elements, one on each face. The stresses are evaluated at a set of internal points uniformly distributed on a smaller cube inside the boundary. As the size of this smaller cube increases towards $2\text{m} \times 2\text{m} \times 2\text{m}$, the internal point evaluations involve increasingly challenging near-singular integrals. The distance from the internal point to the boundary surface is denoted δ . In order to illustrate the accuracy of the \sinh^+ scheme against the competing methods, an average relative error (ε_{are}) is defined as

$$\varepsilon_{\text{are}} = \frac{1}{N} \sum_{i=1}^N \left| \frac{\sigma_{\text{num}}^i - \sigma_{\text{ref}}^i}{\sigma_{\text{ref}}^i} \right| \quad (82)$$

where N is the number of internal points, and σ_{num}^i (or σ_{ref}^i) represents the numerical (or reference) result at the i th internal point. In this example, the errors are compared to analytical solutions for stress. For stresses at an interior point, a BIE for the stresses (see Appendix B) will be used. Let us remark that hyper near-singular integrals (kernels of order $1/r^3$) arises in the computation.

We consider the distance δ to vary from 0.5 to $1.0 \times 10^{-6}\text{m}$, so that the aspect ratio d^* varies from 0.25 to 0.5×10^{-6} . The average relative errors (ε_{are}) in the normal stress σ_x for the internal point set are shown in Fig. 22, comparing the \sinh^+ , \sinh transformation and adaptive schemes. It is evident that for $d^* > 10^{-3}$ all methods can deliver highly accurate results. It is evident that the \sinh^+ and conventional \sinh transformation can produce very accurate results using only six isogeometric elements with d^* as low as 1.0×10^{-7} . For this example containing only planar surfaces, the NURBS geometric description degenerates to become a B-spline and the truncation error in Eqs. (41) and (51) vanishes. It is for this reason that the \sinh^+ scheme and conventional \sinh transformation method offer the same accuracy.

In Fig. 23, the CPU time requirements of the different schemes are presented. For large d^* the adaptive integral method is adopted for all the computations of what is a regular integral, and this results in the CPU time of the three methods being very similar. As d^* reduces to 0.1 and below, the CPU time requirement for the adaptive scheme increases sharply, to the extent that the method was not used in the tests for $d^* < 0.005$. The CPU time of the \sinh^+ scheme remains fixed at around 130s . Owing to the overhead in selecting the appropriate integration scheme, computing the minimum distance and finding the element divide point (shown in Fig. 14), \sinh^+ requires approximately 15% more CPU time than the classical \sinh transformation in the small d^* regime.

6.4. Thick-walled pipeline

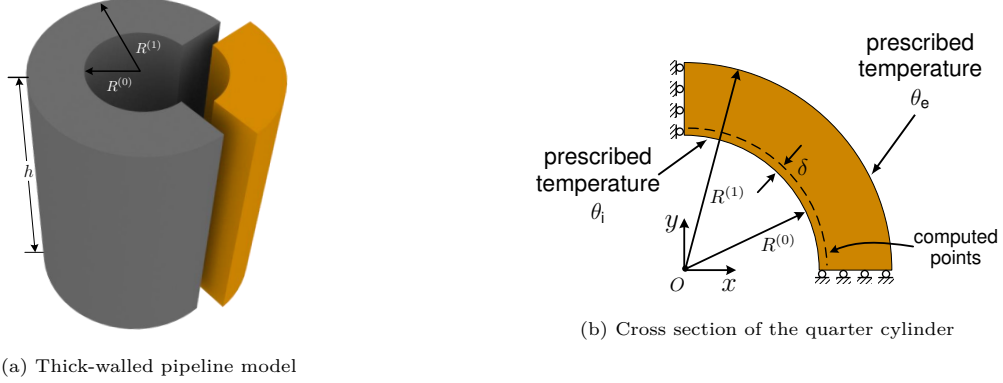


Figure 24: Thin-walled quarter cylinder model

To illustrate the accuracy and effectiveness of the 3D IGABEM using the new \sinh^+ scheme for a problem including a curved boundary, a thermoelastic problem in a thick-walled pipeline as shown in Fig. 24a is studied. The pipeline is made of a superalloy (GH4033) with material properties are as follows: Young's modulus $E = 220\text{GPa}$, Poisson's ratio $\nu = 0.3$, thermal conductivity $k = 10.9\text{W/m} \cdot \text{K}$ and thermal-expansion coefficient $\alpha = 11.56 \times 10^{-6} \text{ } ^\circ\text{C}^{-1}$. The inner surface is maintained at a temperature θ_i , and the outer surface is maintained at a temperature θ_e . The flat ends of the cylinder are taken to be thermally insulated, i.e. $\nabla\theta \cdot \mathbf{n} = 0$, so that the heat conduction becomes purely radial. Geometric dimensions of the model are $R^{(0)} = 2.0\text{m}$, $R^{(1)} = 4.0\text{m}$ and $h = 6.0\text{m}$. The original parametric definition of the model is given in Appendix A. An internal point set is uniformly distributed on an interior surface (the dashed line in Fig. 24b), a distance δ from the inner surface of the cylinder so that the coordinates of the internal points are

$$x = (R^{(0)} + \delta) \cos(\psi); y = (R^{(0)} + \delta) \sin(\psi); z = t \quad (83)$$

where we take $0 < \psi < \pi/2$, $0 < t < 6\text{m}$, and the distance δ varying from 0.5m to 10^{-7}m . The temperatures on the inner and outer cylinder surfaces are prescribed as $\theta_i = 100^\circ\text{C}$ and $\theta_e = 70^\circ\text{C}$, respectively.

We exploit the planes of symmetry of the problem to restrict the analysis domain to a quarter cylinder (the orange part in Fig. 24a); the boundary conditions are shown in Fig. 24b. Six isogeometric elements are used to discretize the model, one on each surface. The end caps are constrained against axial displacement, so plane strain conditions prevail allowing the use of an analytical solution [82, 83] as the reference solution for temperature and displacement (see Appendix C). Here, the errors are compared to analytical solutions for displacement.

In Fig. 25, we present the average relative error ε_{are} in the radial displacement as the internal point set approaches the inner surface; the errors are shown as a function of δ . The corresponding CPU time requirements are compared in Fig. 26. Due to the use of a NURBS geometric description, the truncation error in Eqs. (41) and (51) is no longer zero, and some different conclusions from Section 6.1 are drawn. As expected, the new \sinh^+ scheme, \sinh transformation and adaptive method can all deliver accurate results for larger values of δ , though the range of practical applicability of the adaptive method is limited to $\delta > 10^{-2}$ because of the growth in its CPU time requirements. The \sinh^+ scheme can still deliver accurate results, with relative errors around 10^{-3} for distance δ as small as 10^{-7}m . The truncation error causes the \sinh transformation to lose some accuracy, its relative errors stabilizing around 10^{-2} for small δ . The CPU time requirements of the new \sinh^+ and \sinh transformation schemes remain stable down to $\delta = 10^{-7}$. We conclude that for this problem the \sinh^+ scheme provides consistently good results, with approximately one order of magnitude reduction in error, in comparison with the \sinh transformation, but with a somewhat increased run time.

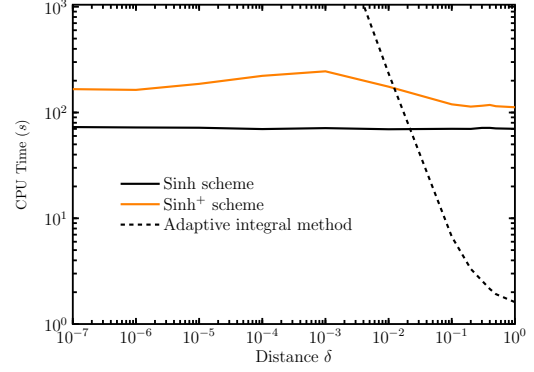
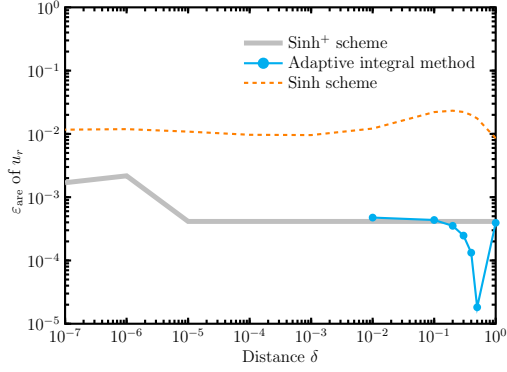


Figure 25: ϵ_{are} of radial displacement u_r at the internal points Figure 26: Comparisons of CPU time for different methods

6.5. Thermoelastic problem for cylinder model with multilayered coating structures

In this example, we consider a multilayered cylinder model under radial temperature variation in plane strain. As shown in Fig. 27, the model involves a superalloy substrate with inner and outer radii $r_1, r_2 = 2, 5\text{m}$. At the inner and outer radii the substrate is covered by a thermal barrier coating (TBC) of thickness δm . The TBC is made of YSZ (Y_2O_3 -stabilized ZrO_2), a widely used TBC material for high-temperature applications such as diesel engines and gas turbines [1, 3]. The substrate is made of superalloy GH4033 having a Young's modulus $E = 220\text{GPa}$, a Poisson's ratio $\nu = 0.3$, a thermal conductivity $k = 10.9 \text{ W/m}\cdot\text{K}$ and a thermal-expansion coefficient $\alpha = 11.56 \times 10^{-6} \text{ }^\circ\text{C}^{-1}$. The material constants for the YSZ coating are taken as: Young's modulus $E = 48\text{GPa}$, Poisson's ratio $\nu = 0.25$, thermal conductivity $k = 2.3 \text{ W/m}\cdot\text{K}$ and thermal-expansion coefficient $\alpha = 11 \times 10^{-6} \text{ }^\circ\text{C}^{-1}$. Once again, a quarter-symmetrical model of the cylinder is used (as shown in Fig. 27a) and the boundary conditions are given in Fig. 27b. The flat ends of the cylinder model are assumed thermally insulated, i.e. $\nabla\theta \cdot \mathbf{n} = 0$, and are constrained against axial displacement.

In the computation, the coating thickness δ varies from 0.5 to 10^{-7}m . The temperatures on the inner and outer surfaces are prescribed as boundary conditions, with $\theta_1 = 120^\circ\text{C}$ and $\theta_4 = 80^\circ\text{C}$. The plane strain conditions allow the reference solution to be taken from an analytical solution for displacement and temperature [82, 83] using the formulations given in Appendix C with three layers. In this example, the errors are compared to analytical solutions for displacement and temperature.

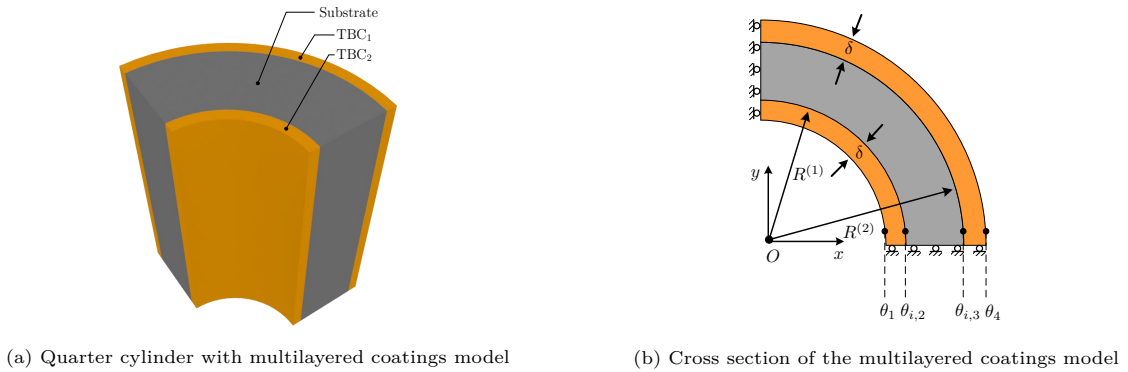


Figure 27: Multilayered coatings model

Figs. 28a and 28b show the L^2 relative error norms, $E_2(u_r; \Gamma_{\text{int}1})$ and $E_2(\theta; \Gamma_{\text{int}2})$, of the radial displacements, u_r , and temperatures respectively, for coating thicknesses down to 10^{-7}m . Here, the interface between TBC_1 and substrate is denoted $\Gamma_{\text{int}1}$ and the interface between substrate and TBC_2 is denoted

$\Gamma_{\text{int}2}$. Once again, the new \sinh^+ scheme outperforms the conventional \sinh scheme, being able to deliver accurate results from coating models containing as few as six isogeometric elements, and being stable at very small coating thicknesses. Fig. 29 presents the effect of ϵps on the same error norms when 6 Taylor series terms are used in Eq. (41). The influence of the tolerance ϵps can be clearly seen for 6 isogeometric elements, with both $E_2(u_r; \Gamma_{\text{int}1})$ and $E_2(\theta; \Gamma_{\text{int}2})$ stabilising as ϵps reduces. It should be noted that when the values of $\epsilon ps \gg 10^{-1}$, the \sinh^+ scheme will become the conventional \sinh scheme.

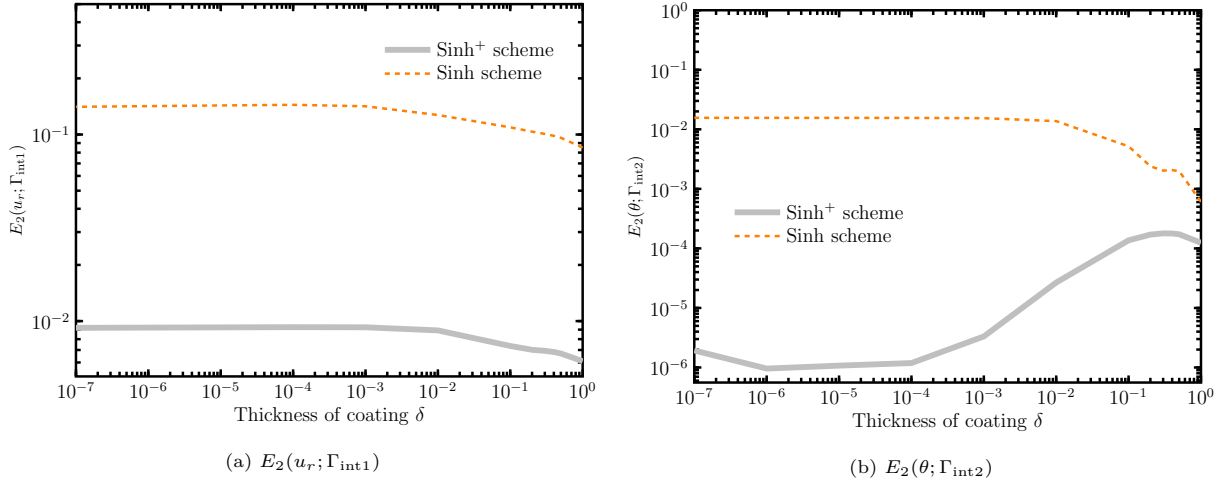


Figure 28: L^2 relative error norm of radial displacement and temperature on the interface

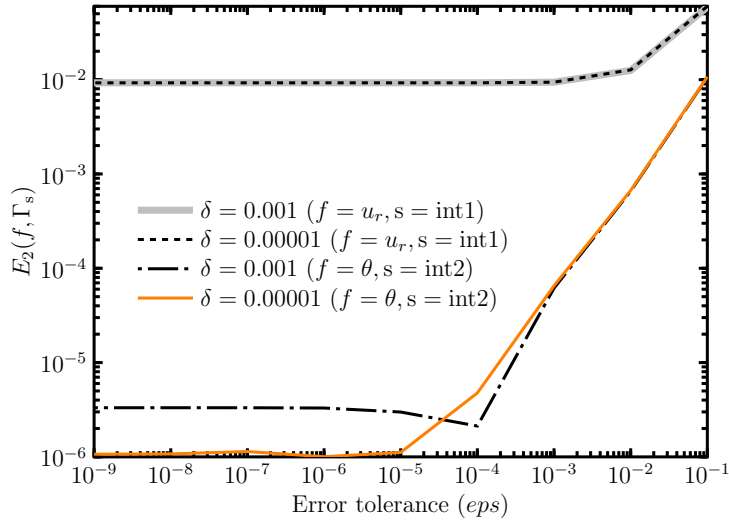


Figure 29: L^2 relative error norm $E_2(f; \Gamma_s)$ when different error tolerances (ϵps) are used in \sinh^+ scheme

Finally, using the initial parameters (6 isogeometric elements), the temperature distribution inside the substrate (surface on $z = 4$) and its relative error for coating thickness $\delta = 10^{-6}$ are given in Figs. 30a and 30b respectively.

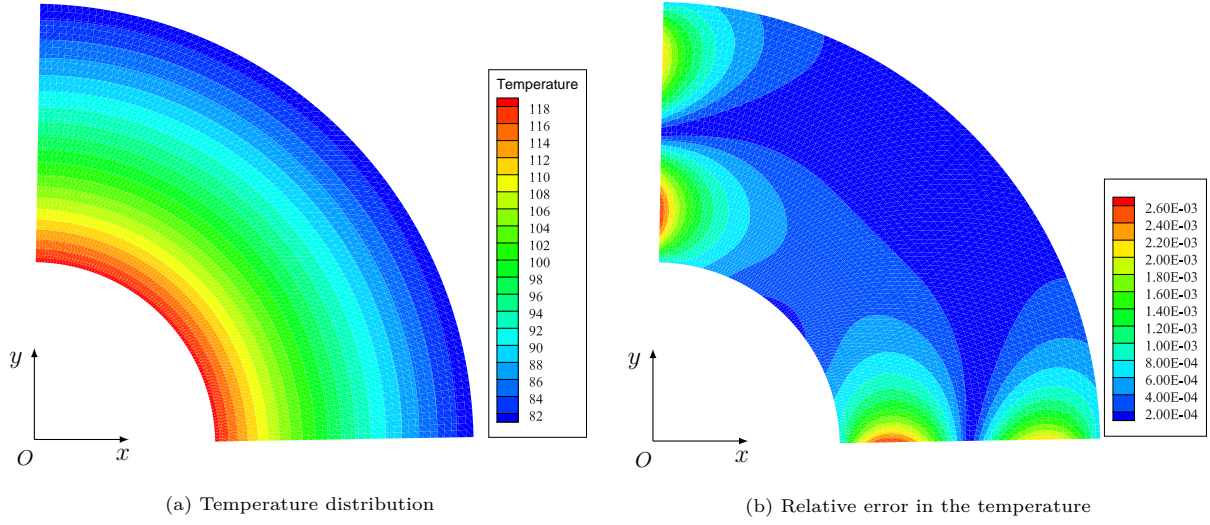


Figure 30: Temperature distribution and its relative error with $\delta = 10^{-6}$

6.6. Nozzle structure

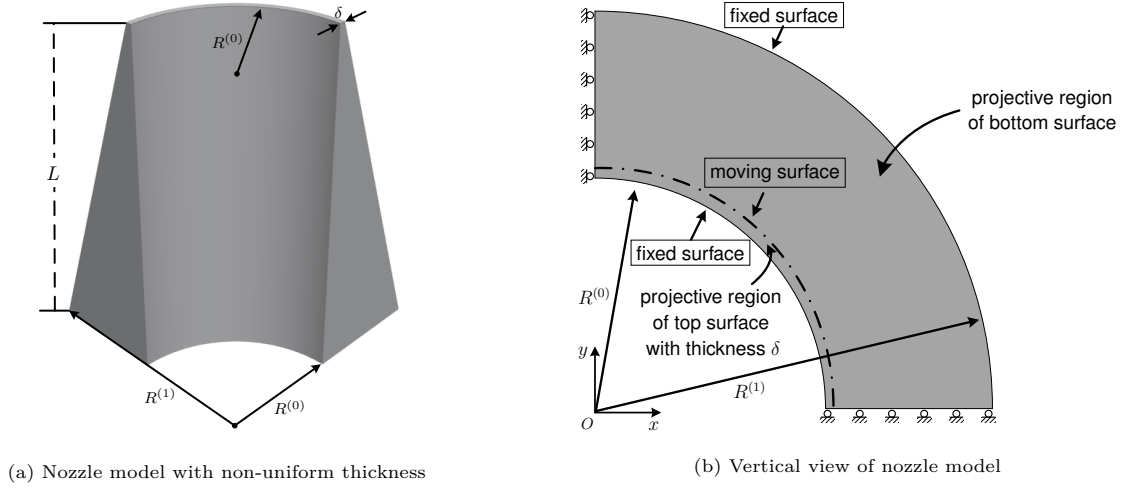


Figure 31: The computed nozzle model

In the final example, we present a quarter-symmetric analysis of a nozzle formed from a truncated cone with an axial cylindrical drilling, as illustrated in Figs. 31a and 31b. The inner and outer radii of the fixed base are $R^{(0)} = 2\text{mm}$ and $R^{(1)} = 6\text{mm}$, respectively and the height $L = 6\text{mm}$. The inner radius of the top surface remains $R^{(0)}$, and the radial thickness of the top surface, δ , is allowed to vary from 0.5 to 10^{-7}mm . These are simple and widely used geometries, and present significant challenges to engineers using the conventional BEM and FEM as well as isogeometric formulations. The temperature distribution $\theta = 10^6(x + y)$, with x and y measured in m, is prescribed as a boundary condition on the inner and outer surfaces.

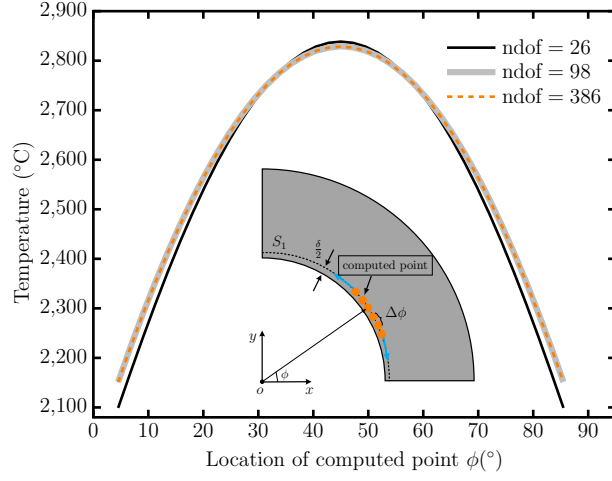


Figure 32: Temperature distribution along curve S_1 for different ndofs

In Fig. 32 we present the temperature distribution over the contour S_1 for the case $\delta = 8.0 \times 10^{-5}$ mm. Three different model refinements are shown, and the contour S_1 , which is illustrated in the Figure, is defined by

$$S_1 = \left\{ (x, y, z) : x = \left(R^{(0)} + \frac{\delta}{2} \right) \cos \phi, y = \left(R^{(0)} + \frac{\delta}{2} \right) \sin \phi, z = 0.6\text{mm}, \phi \in \left(0, \frac{\pi}{2} \right) \right\} \quad (84)$$

From Fig. 32, we can see that a model containing only 26 degrees of freedom is too coarse to provide a good solution for the temperature, but the results are much improved with 98 degrees of freedom. The convergence can be clearly seen even though the thickness of the the top surface is only $0.08\mu\text{m}$ and the distance from internal points on S_1 to the inner surface is $0.04\mu\text{m}$.

Fig. 33 shows the computed temperature at points lying on the contour S_2 , which has the same x and y parameters as S_1 , but with a coordinate $z = 5.4\text{mm}$ the contour is close to the top surface, where the thickness of the section is very small. Here, the temperature distribution obtained from the 98 degree of freedom model shows more significant errors, but with model refinement the results converge well to a stable solution.

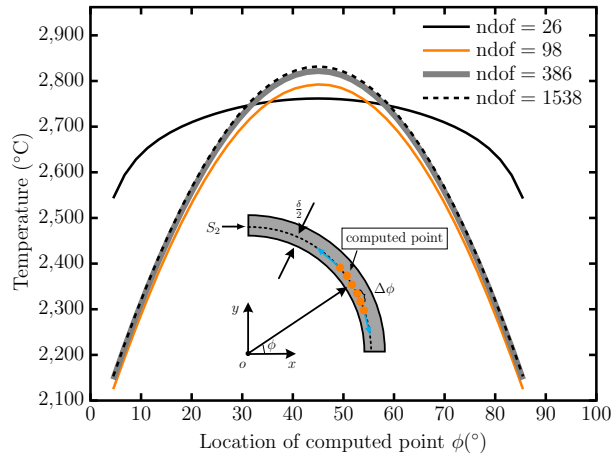


Figure 33: Temperature distribution along curve S_2 for different mesh refinements

7. Conclusion

In this paper, some 3D thermoelastic problems in engineering systems with thermal barrier coatings and thin structures have been studied using the 3D Isogeometric Boundary Element Method (IGABEM). With its boundary-only analysis model aligning well with CAD descriptions and its attractive convergence properties, IGABEM is a very promising method for a fully integrated CAD/CAE environment. However, the existence of large numbers of near-singular integrals poses challenges for the numerical implementation with standard quadrature schemes for problems containing coated structures or other thin sections.

Existing methods for evaluating near-singular integrals over a surface isogeometric element have been evaluated, and it has been shown that it is impossible to achieve a satisfactory balance between accuracy and efficiency simultaneously by using only one of the these existing approaches. We propose a new \sinh^+ scheme which is a hybrid of \sinh transformation and adaptive integration methods. The analytical extension of the NURBS surface is used to extend the \sinh transformation in order to cope with cases in which the projections of source points or internal points lie outside the domain of the element over which the integration is taken. This enhances the robustness of the scheme.

The new scheme is able to deliver results of good accuracy and with good computational efficiency. One feature of the scheme is that it allows engineers to balance the computation accuracy and efficiency by changing the tolerance ϵ_{ps} or choosing a values of d_{crit}^* as may be required for different cases. The numerical results show that the scheme has been successfully developed for weakly, strongly and hyper near-singular kernels.

This work focuses on the implementation and error analysis of the presented integral scheme. In the future work, the authors will discuss the mesh convergence coupled with the integration convergence. The Geometry-Independent Field approximation (GIFT) method [11], which will be a possible way to perform local refinement using NURBS for the geometry and other splines for the field variables may be adopted.

Acknowledgements

The authors acknowledge the support from the National Natural Science Foundation of China (11672038, 11972085) and the Beijing Key Laboratory of Advanced Manufacturing Technology. The author Yanpeng Gong would also like to thank Dr Kaizhou Lu for his comments on the pictures.

References

- [1] N. P. Padture, M. Gell, E. H. Jordan, Thermal barrier coatings for gas-turbine engine applications, *Science* 296 (5566) (2002) 280–284.
- [2] Y. Gong, J. Trevelyan, G. Hattori, C. Dong, Hybrid nearly singular integration for isogeometric boundary element analysis of coatings and other thin 2D structures, *Computer Methods in Applied Mechanics and Engineering* 346 (2019) 642–673.
- [3] X. Q. Cao, R. Vassen, D. Stoeber, Ceramic materials for thermal barrier coatings, *Journal of the European Ceramic Society* 24 (1) (2004) 1 – 10.
- [4] A. G. Evans, J. W. Hutchinson, The mechanics of coating delamination in thermal gradients, *Surface and Coatings Technology* 201 (18) (2007) 7905 – 7916.
- [5] M.-J. Pindera, J. Aboudi, S. M. Arnold, Analysis of spallation mechanism in thermal barrier coatings with graded bond coats using the higher-order theory for FGMs, *Engineering Fracture Mechanics* 69 (14) (2002) 1587 – 1606.
- [6] M. Białas, Finite element analysis of stress distribution in thermal barrier coatings, *Surface and Coatings Technology* 202 (24) (2008) 6002 – 6010.
- [7] P. Skalka, K. Slámečka, J. Pokluda, L. Čelko, Stability of plasma-sprayed thermal barrier coatings: The role of the waviness of the bond coat and the thickness of the thermally grown oxide layer, *Surface and Coatings Technology* 274 (2015) 26 – 36.
- [8] L. Yang, Q. Liu, Y. Zhou, W. Mao, C. Lu, Finite element simulation on thermal fatigue of a turbine blade with thermal barrier coatings, *Journal of Materials Science & Technology* 30 (4) (2014) 371 – 380.
- [9] T. J. R. Hughes, J. A. Cottrell, Y. Bazilevs, Isogeometric analysis: CAD, finite elements, NURBS, exact geometry and mesh refinement, *Computer Methods in Applied Mechanics and Engineering* 194 (39–41) (2005) 4135–4195.
- [10] A. I. Grebennikov, Isogeometric approximation of functions of one variable, *USSR Computational Mathematics and Mathematical Physics* 22 (6) (1982) 42–50.
- [11] E. Atroshchenko, S. Tomar, G. Xu, S. P. Bordas, Weakening the tight coupling between geometry and simulation in isogeometric analysis: From sub- and super-geometric analysis to geometry-independent field approximation (GIFT), *International Journal for Numerical Methods in Engineering* 114 (10) (2018) 1131–1159.

- [12] G. Xu, M. Li, B. Mourrain, T. Rabczuk, J. Xu, S. P. A. Bordas, Constructing IGA-suitable planar parameterization from complex CAD boundary by domain partition and global/local optimization (2017). [arXiv:1707.00607](#).
- 515 [13] G. Xu, B. Mourrain, R. Duvigneau, A. Galligo, Optimal analysis-aware parameterization of computational domain in isogeometric analysis, in: B. Mourrain, S. Schaefer, G. Xu (Eds.), *Advances in Geometric Modeling and Processing*, Springer Berlin Heidelberg, Berlin, Heidelberg, 2010, pp. 236–254.
- [14] E. Pilgerstorfer, B. Jüttler, Bounding the influence of domain parameterization and knot spacing on numerical stability in isogeometric analysis, *Computer Methods in Applied Mechanics and Engineering* 268 (2014) 589 – 613.
- 520 [15] Q. Hu, F. Chouly, P. Hu, G. Cheng, S. Bordas, Skew-symmetric nitsche's formulation in isogeometric analysis: Dirichlet and symmetry conditions, patch coupling and frictionless contact, *Computer Methods in Applied Mechanics and Engineering* 341 (2018).
- [16] V. P. Nguyen, C. Anitescu, S. P. Bordas, T. Rabczuk, Isogeometric analysis: An overview and computer implementation aspects, *Mathematics and Computers in Simulation* 117 (2015) 89 – 116.
- 525 [17] A. Yadav, R. Godara, G. Bhardwaj, A review on XIGA method for computational fracture mechanics applications, *Engineering Fracture Mechanics* 230 (2020) 107001.
- [18] H. Lian, S. Bordas, R. Sevilla, Recent developments in CAD/analysis integration, *Computational Technology Reviews* 6 (2012) 1–36.
- [19] S. P. A. Bordas, T. Rabczuk, J. J. Rodenas, P. Kerfriden, S. Belouettar, Recent advances towards reducing the meshing and re-meshing burden in computational sciences, *Computational Technology Reviews* 2 (2010) 51–82.
- 530 [20] R. N. Simpson, S. P. Bordas, J. Trevelyan, T. Rabczuk, A two-dimensional isogeometric boundary element method for elastostatic analysis, *Computer Methods in Applied Mechanics and Engineering* 209 (2012) 87–100.
- [21] R. Simpson, S. Bordas, H. Lian, J. Trevelyan, An isogeometric boundary element method for elastostatic analysis: 2D implementation aspects, *Computers & Structures* 118 (2013) 2 – 12.
- 535 [22] H. Lian, R. N. Simpson, S. P. A. Bordas, Stress analysis without meshing: isogeometric boundary-element method, *Proceedings of the Institution of Civil Engineers - Engineering and Computational Mechanics* 166 (2) (2013) 88–99.
- [23] X. Peng, E. Atroshchenko, S. P. Bordas, Damage tolerance assessment directly from CAD: (extended)isogeometric boundary element methods (XIGABEM), in: *Book of abstracts of the 6th International Conference on Advanced Computational Methods in Engineering*, 2014.
- 540 [24] L. Chen, S. Marburg, W. Zhao, C. Liu, H. Chen, Implementation of isogeometric fast multipole boundary element methods for 2D half-space acoustic scattering problems with absorbing boundary condition, *Journal of Theoretical and Computational Acoustics* 27 (02) (2019) 1850024.
- [25] X. Peng, E. Atroshchenko, P. Kerfriden, S. Bordas, Isogeometric boundary element methods for three dimensional static fracture and fatigue crack growth, *Computer Methods in Applied Mechanics and Engineering* 316 (2017) 151 – 185.
- 545 [26] G. Beer, B. Marussig, C. Duenser, The Isogeometric Boundary Element Method. *Lecture Notes in Applied and Computational Mechanics*, Vol. 90, Springer, Cham, 2020.
- [27] Y. Gu, W. Chen, C. Zhang, Stress analysis for thin multilayered coating systems using a sinh transformed boundary element method, *International Journal of Solids and Structures* 50 (20) (2013) 3460 – 3471.
- [28] Y. Gu, X. He, W. Chen, C. Zhang, Analysis of three-dimensional anisotropic heat conduction problems on thin domains using an advanced boundary element method, *Computers & Mathematics with Applications* 75 (1) (2018) 33 – 44.
- 550 [29] J. Baynham, R. Adey, V. Murugaian, D. Williams, Simulating electro-coating of automotive body parts using BEM, *WIT Transactions on Engineering Sciences* 54 (2007) 89–99.
- [30] H. L. Zhou, H. S. Han, C. Z. Cheng, Z. R. Niu, Inverse identification of heat boundary conditions for 2-D anisotropic coating structures, in: *Mechanical and Electronics Engineering III*, Vol. 130 of *Applied Mechanics and Materials*, Trans Tech Publications Ltd, 2012, pp. 1825–1828.
- 555 [31] Y.-M. Zhang, Y. Gu, J.-T. Chen, Stress analysis for multilayered coating systems using semi-analytical BEM with geometric non-linearities, *Computational Mechanics* 47 (5) (2011) 493–504.
- [32] Y. C. Shiah, Y. X. Shi, Heat conduction across thermal barrier coatings of anisotropic substrates, *International Communications in Heat & Mass Transfer* 33 (7) (2006) 827–835.
- 560 [33] X. Chen, Y. Liu, Thermal stress analysis of multi-layer thin films and coatings by an advanced boundary element method, *CMES - Computer Modeling in Engineering and Sciences* 2 (3) (2001) 337–349.
- [34] J. Gu, J. Zhang, G. Li, Isogeometric analysis in BIE for 3-D potential problem, *Engineering Analysis with Boundary Elements* 36 (5) (2012) 858–865.
- [35] V. Sladek, J. Sladek, Singular integrals and boundary elements, *Computer Methods in Applied Mechanics and Engineering* 157 (3-4) (1998) 251–266.
- 565 [36] G. S. Padhi, R. A. Shenoi, S. S. J. Moy, M. A. McCarthy, Analytic integration of kernel shape function product integrals in the boundary element method, *Computers & Structures* 79 (14) (2001) 1325–1333.
- [37] Z. Niu, C. Cheng, H. Zhou, Z. Hu, Analytic formulations for calculating nearly singular integrals in two-dimensional BEM, *Engineering Analysis with Boundary Elements* 31 (12) (2007) 949–964.
- 570 [38] H. Zhou, Z. Niu, C. Cheng, Z. Guan, Analytical integral algorithm applied to boundary layer effect and thin body effect in BEM for anisotropic potential problems, *Computers & structures* 86 (15-16) (2008) 1656–1671.
- [39] V. Sladek, J. Sladek, M. Tanaka, Numerical integration of logarithmic and nearly logarithmic singularity in BEMs, *Applied Mathematical Modelling* 25 (11) (2001) 901–922.
- 575 [40] Z. Niu, W. L. Wendland, X. Wang, H. Zhou, A semi-analytical algorithm for the evaluation of the nearly singular integrals in three-dimensional boundary element methods, *Computer Methods in Applied Mechanics and Engineering* 194 (9-11) (2005) 1057–1074.
- [41] J. C. F. Telles, A self-adaptive co-ordinate transformation for efficient numerical evaluation of general boundary element

integrals, *International Journal for Numerical Methods in Engineering* 24 (5) (1987) 959–973.

- [42] K. Hayami, H. Matsumoto, A numerical quadrature for nearly singular boundary element integrals, *Engineering Analysis with Boundary Elements* 13 (2) (1994) 143–154.
- [43] G. Krishnasamy, F. J. Rizzo, Y. Liu, Boundary integral equations for thin bodies, *International Journal for Numerical Methods in Engineering* 37 (1) (1994) 107–121.
- [44] Y. Liu, Analysis of shell-like structures by the boundary element method based on 3-D elasticity: formulation and verification, *International Journal for Numerical Methods in Engineering* 41 (3) (1998) 541–558.
- [45] Y. J. Liu, D. M. Zhang, F. J. Rizzo, Nearly singular and hypersingular integrals in the boundary element method, *WIT Transactions on Modelling and Simulation* 1 (1970).
- [46] E. Lutz, Exact Gaussian quadrature methods for near-singular integrals in the boundary element method, *Engineering Analysis with Boundary Elements* 9 (3) (1992) 233–245.
- [47] Y. C. Wang, H. Q. Li, H. B. Chen, Y. Wu, Particular solutions method to adjust singularity for the calculation of stress and displacement at arbitrary point, *Acta Mechanica Sinica* (1994) 02.
- [48] H. B. Chen, Y. C. Wang, P. Lu, Stress rate integral equations of elastoplasticity, *Acta Mechanica Sinica* 12 (1) (1996) 55–64.
- [49] X.-W. Gao, T. G. Davies, Adaptive integration in elasto-plastic boundary element analysis, *Journal of the Chinese institute of engineers* 23 (3) (2000) 349–356.
- [50] X.-W. Gao, T. G. Davies, *Boundary element programming in mechanics*, Cambridge University Press, 2002.
- [51] M. Tanaka, V. Sladek, J. Sladek, Regularization techniques applied to boundary element methods, *Applied Mechanics Reviews* 47 (10) (1994) 457–499.
- [52] J. F. Luo, Y. J. Liu, E. J. Berger, Analysis of two-dimensional thin structures (from micro-to nano-scales) using the boundary element method, *Computational Mechanics* 22 (5) (1998) 404–412.
- [53] H. Ma, N. Kamiya, Domain supplemental approach to avoid boundary layer effect of BEM in elasticity, *Engineering Analysis with Boundary Elements* 23 (3) (1999) 281–284.
- [54] H. Ma, N. Kamiya, A general algorithm for the numerical evaluation of nearly singular boundary integrals of various orders for two-and three-dimensional elasticity, *Computational Mechanics* 29 (4-5) (2002) 277–288.
- [55] X. Qin, J. Zhang, G. Xie, F. Zhou, G. Li, A general algorithm for the numerical evaluation of nearly singular integrals on 3D boundary element, *Journal of Computational and Applied Mathematics* 235 (14) (2011) 4174–4186.
- [56] J. Zhang, P. Wang, C. Lu, Y. Dong, A spherical element subdivision method for the numerical evaluation of nearly singular integrals in 3D BEM, *Engineering Computations* 34 (6) (2017) 2074–2087.
- [57] B. M. Johnston, P. R. Johnston, D. Elliott, A sinh transformation for evaluating two-dimensional nearly singular boundary element integrals, *International Journal for Numerical Methods in Engineering* 69 (7) (2007) 1460–1479.
- [58] J. Lv, Y. Miao, H. Zhu, The distance sinh transformation for the numerical evaluation of nearly singular integrals over curved surface elements, *Computational Mechanics* 53 (2) (2014) 359–367.
- [59] Y. Zhang, Y. Gong, X. Gao, Calculation of 2D nearly singular integrals over high-order geometry elements using the sinh transformation, *Engineering Analysis with Boundary Elements* 60 (2015) 144–153.
- [60] G. Xie, F. Zhou, J. Zhang, X. Zheng, C. Huang, New variable transformations for evaluating nearly singular integrals in 3D boundary element method, *Engineering Analysis with Boundary Elements* 37 (9) (2013) 1169 – 1178.
- [61] G. Xie, J. Zhang, Y. Dong, C. Huang, G. Li, An improved exponential transformation for nearly singular boundary element integrals in elasticity problems, *International Journal of Solids and Structures* 51 (6) (2014) 1322–1329.
- [62] Y. Zhang, X. Li, V. Sladek, J. Sladek, X. Gao, A new method for numerical evaluation of nearly singular integrals over high-order geometry elements in 3D BEM, *Journal of Computational and Applied Mathematics* 277 (2015) 57 – 72.
- [63] L. C. Wrobel, C. A. Brebbia, *Boundary Element Methods in Heat Transfer*, Springer, Dordrecht, 1992.
- [64] A. A. Becker, *The Boundary Element Method in Engineering: A Complete Course*, McGraw-Hill Companies, 1992.
- [65] G. Beer, I. Smith, C. Duenser, *The Boundary Element Method with Programming: For Engineers and Scientists*, Springer-Verlag Wien, 2008.
- [66] V. Takhteyev, C. A. Brebbia, Analytical integrations in boundary elements, *Engineering Analysis with Boundary Elements* 7 (2) (1990) 95–100.
- [67] X.-W. Gao, The radial integration method for evaluation of domain integrals with boundary-only discretization, *Engineering Analysis with Boundary Elements* 26 (10) (2002) 905–916.
- [68] F. J. Rizzo, D. J. Shippy, An advanced boundary integral equation method for three-dimensional thermoelasticity, *International Journal for Numerical Methods in Engineering* 11 (11) (1977) 1753–1768.
- [69] P. W. Partridge, C. A. Brebbia, L. C. Wrobel, *The dual reciprocity boundary element method*, Springer, Dordrecht, 1992.
- [70] L. Piegl, W. Tiller, *The NURBS Book*, Springer-Verlag Berlin Heidelberg, 1995.
- [71] J. A. Cottrell, T. J. R. Hughes, Y. Bazilevs, *Isogeometric Analysis: Toward Integration of CAD and FEA*, John Wiley & Sons, Ltd, 2009.
- [72] J. T. Katsikadelis, *Boundary Elements: Theory and Applications*, 1st Edition, Elsevier Science, 2002.
- [73] Y. P. Gong, H. S. Yang, C. Y. Dong, A novel interface integral formulation for 3D steady state thermal conduction problem for a medium with non-homogenous inclusions, *Computational Mechanics* 63 (2) (2019) 181–199.
- [74] T. N. E. Greville, Numerical procedures for interpolation by spline functions, *Journal of the Society for Industrial & Applied Mathematics* 1 (3) (1964) 53–68.
- [75] Y. P. Gong, C. Y. Dong, X. C. Qin, An isogeometric boundary element method for three dimensional potential problems, *Journal of Computational and Applied Mathematics* 313 (2017) 454–468.
- [76] X.-W. Gao, An effective method for numerical evaluation of general 2D and 3D high order singular boundary integrals, *Computer Methods in Applied Mechanics and Engineering* 199 (45–48) (2010) 2856–2864.

- [77] G. G. W. Mustoe, Advanced integration schemes over boundary elements and volume cells for two-and three-dimensional non-linear analysis, *Developments in Boundary Element Methods* 3 (1984) 213–270.
- [78] S. Bu, T. G. Davies, Effective evaluation of non-singular integrals in 3D BEM, *Advances in Engineering Software* 23 (2) (1995) 121–128.
- [79] Y. P. Gong, C. Y. Dong, An isogeometric boundary element method using adaptive integral method for 3D potential problems, *Journal of Computational and Applied Mathematics* 319 (2017) 141–158.
- [80] Y. P. Gong, C. Y. Dong, X. Y. Qu, An adaptive isogeometric boundary element method for predicting the effective thermal conductivity of steady state heterogeneity, *Advances in Engineering Software* 119 (2018) 103–115.
- [81] J. Telles, R. Oliveira, Third degree polynomial transformation for boundary element integrals: Further improvements, *Engineering Analysis with Boundary Elements* 13 (2) (1994) 135 – 141.
- [82] F. Carannante, some new thermo-elastic solutions for cylindrical and spherical composites, phdthesis, Università degli studi di Napoli Federico II (Feb. 2013).
- [83] L.-Y. Chen, Y. Li, H. Jiang, General computation method for axisymmetric temperature and thermal stress of multilayer cylinder, *Journal of materials and metallurgy* 6 (4) (2007) 297–315.

A. Appendix: Parameter definition of quarter cylinder

As shown in Fig.34, the quarter cylinder is constructed by 6 patches. The original parametric definition of each patch is given by $\Xi = \{0, 0, 0, 1, 1, 1\}$ and $\mathcal{H} = \{0, 0, 0, 1, 1, 1\}$. The control points and weights of all patches are listed in Table 4. The model studied in this work can be obtained by changing coordinates of control points of several patches.

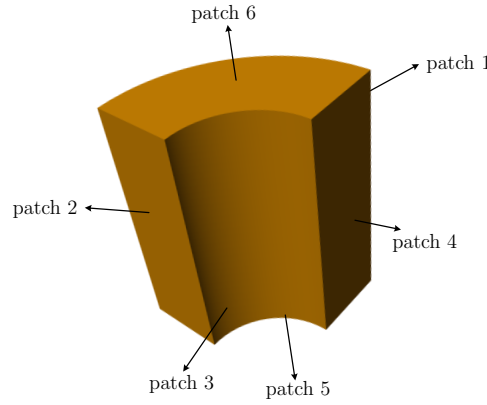


Figure 34: Model Construction of quarter cylinder

Table 4: Control points and weights of each patch (x_1, x_2, x_3 , weight)

control ponts	1	2	3	4	5	6	7	8	9
patch 1	(5,0,6,1)	(5,0,3,1)	(5,0,0,1)	(5,5,6, $\frac{\sqrt{2}}{2}$)	(5,5,3, $\frac{\sqrt{2}}{2}$)	(5,5,0, $\frac{\sqrt{2}}{2}$)	(0,5,6,1)	(0,5,3,1)	(0,5,0,1)
patch 2	(0,5,6,1)	(0,5,3,1)	(0,5,0,1)	(0, $\frac{7}{2}$,6,1)	(0, $\frac{7}{2}$,3,1)	(0, $\frac{7}{2}$,0,1)	(0,2,6,1)	(0,2,3,1)	(0,2,0,1)
patch 3	(0,2,6,1)	(0,2,3,1)	(0,2,0,1)	(2,2,6, $\frac{\sqrt{2}}{2}$)	(2,2,3, $\frac{\sqrt{2}}{2}$)	(2,2,0, $\frac{\sqrt{2}}{2}$)	(2,0,6,1)	(2,0,3,1)	(2,0,0,1)
patch 4	(2,0,6,1)	(2,0,3,1)	(2,0,0,1)	($\frac{7}{2}$,0,6,1)	($\frac{7}{2}$,0,3,1)	($\frac{7}{2}$,0,0,1)	(5,0,6,1)	(5,0,3,1)	(5,0,0,1)
patch 5	(0,5,0,1)	(5,5,0, $\frac{\sqrt{2}}{2}$)	(5,0,0,1)	(0, $\frac{7}{2}$,0,1)	($\frac{7}{2}$, $\frac{7}{2}$,0, $\frac{\sqrt{2}}{2}$)	($\frac{7}{2}$,0,0,1)	(0,2,0,1)	(2,2,0, $\frac{\sqrt{2}}{2}$)	(2,0,0,1)
patch 6	(0,2,6,1)	(2,2,6, $\frac{\sqrt{2}}{2}$)	(2,0,6,1)	(0, $\frac{7}{2}$,6,1)	($\frac{7}{2}$, $\frac{7}{2}$,6, $\frac{\sqrt{2}}{2}$)	($\frac{7}{2}$,0,6,1)	(0,5,6,1)	(5,5,6, $\frac{\sqrt{2}}{2}$)	(5,0,6,1)

B. Appendix: boundary integral equation for thermal stresses

The BIE for thermal stresses at an interior point \mathbf{y} can be obtained by differentiating the BIE for displacement at point \mathbf{y} and substituting in Hooke's law as follows:

$$\begin{aligned}\sigma_{ij}(\mathbf{y}) = & \int_{\Gamma} D_{kij}(\mathbf{y}, \mathbf{x}) t_k(\mathbf{x}) d\Gamma(\mathbf{x}) - \int_{\Gamma} S_{kij}(\mathbf{y}, \mathbf{x}) u_k(\mathbf{x}) d\Gamma(\mathbf{x}) \\ & + \int_{\Gamma} \frac{E\alpha}{1-2v} D_{kij}(\mathbf{y}, \mathbf{x}) n_k(\mathbf{x}) \theta(\mathbf{x}) d\Gamma(\mathbf{x}) \\ & - \int_V \frac{E\alpha}{1-2v} D_{kij}(\mathbf{y}, \mathbf{x}') \theta_{,k}(\mathbf{x}') dV(\mathbf{x}') - \frac{E\alpha}{1-2v} \theta(\mathbf{y}) \delta_{ij}\end{aligned}\quad (85)$$

where the third-order tensors S_{kij} and D_{kij} can be defined as follows:

$$\begin{aligned}S_{kij}(\mathbf{y}, \mathbf{x}) = & \frac{E}{4\pi(1-v)r^3} \left\{ 3 \frac{\partial r}{\partial \mathbf{n}} [(1-2v)\delta_{ij}r_{,k} + v(\delta_{ik}r_{,j} + \delta_{jk}r_{,i}) - 5r_{,i}r_{,j}r_{,k}] \right. \\ & \left. + 3v(r_{,i}r_{,k}n_j + r_{,j}r_{,k}n_i) + (1-2v)(\delta_{ik}n_j + \delta_{jk}n_i + 3r_{,i}r_{,j}n_k) - (1-4v)\delta_{ij}n_k \right\}\end{aligned}$$

and

$$D_{kij}(\mathbf{y}, \mathbf{x}) = \frac{1}{4\pi(1-v)r^2} [(1-2v)(\delta_{ik}r_{,j} + \delta_{jk}r_{,i} - \delta_{ij}r_{,k} + 3r_{,i}r_{,j}r_{,k})]$$

C. Appendix: analytical thermo-elastic solutions for multilayered hollow cylinder

Let us consider a multilayered hollow cylinder composed of n different materials. The internal radius and external radii are denoted $R^{(0)}$ and $R^{(n)}$, respectively. The radius at the interface between the phase i and the phase $(i+1)$ is denoted $R^{(i)}$. The model is subjected to a temperature gradient varying between θ_i at the inner radius and θ_e at the outer radius.

C.1. Temperature in the multilayered hollow cylinder

The general solution of temperature in each phase can be given by

$$\begin{cases} \theta(r) = A_1 \ln r + B_1, & R^{(0)} \leq r \leq R^{(1)} \\ \theta(r) = A_2 \ln r + B_2, & R^{(1)} \leq r \leq R^{(2)} \\ \vdots \\ \theta(r) = A_n \ln r + B_n, & R^{(n-1)} \leq r \leq R^{(n)} \end{cases}$$

The values of A_i and B_i can be computed by

$$A_i = \frac{\theta_{i+1} - \theta_i}{\ln \rho_i^*}, \quad B_i = \frac{\theta_i \ln R^{(i)} - \theta_{i+1} \ln R^{(i-1)}}{\ln \rho_i^*}, \quad i = 1, 2, \dots, n$$

where $\rho_i^* = \frac{R^{(i)}}{R^{(i-1)}}$ and the unknown interface temperatures $\theta_2, \theta_3, \dots, \theta_n$ can be obtained by the following system

$$\begin{cases} -(\beta_1 + 1)\theta_2 + \beta_1\theta_3 = -\theta_1 \\ \theta_2 - (\beta_2 + 1)\theta_3 + \beta_2\theta_4 = 0 \\ \vdots \\ \theta_i - (\beta_i + 1)\theta_{i+1} + \beta_i\theta_{i+2} = 0 \\ \vdots \\ \theta_{n-1} - (\beta_{n-1} + 1)\theta_n = -\beta_{n-1}\theta_{n+1} \end{cases}$$

where $i = 1, 2, \dots, n$; $\theta_1 = \theta_i$ and $\theta_{n+1} = \theta_e$ are known temperatures at the inner and outer surfaces; and

$$\beta_i = \frac{k^{(i+1)}}{k^{(i)}} \frac{\ln \rho_i^*}{\ln \rho_{i+1}^*}, \quad i = 1, 2, \dots, n-1; n > 1$$

$k^{(i)}$ is the thermal conductivity in the i th layer.

C.2. Displacement in the multilayered hollow cylinder

The general solution of displacement in each phase can be described by

$$\begin{cases} u_{r_1} = \phi_1 \frac{1}{r_1} \int_{R^{(0)}}^{r_1} \theta(r) r dr + C_1 r_1 + \frac{C_2}{r_1}; & R^{(0)} \leq r_1 \leq R^{(1)} \\ u_{r_2} = \phi_2 \frac{1}{r_2} \int_{R^{(1)}}^{r_2} \theta(r) r dr + C_3 r_2 + \frac{C_4}{r_2}; & R^{(1)} \leq r_2 \leq R^{(2)} \\ \vdots \\ u_{r_n} = \phi_n \frac{1}{r_n} \int_{R^{(n-1)}}^{r_n} \theta(r) r dr + C_{2n-1} r_n + \frac{C_{2n}}{r_n}; & R^{(n-1)} \leq r_n \leq R^{(n)} \end{cases} \quad (86)$$

where

$$\phi_i = \frac{1 + v_i}{1 - v_i} \alpha_i \quad (87)$$

and

$$\int_{R^{(i-1)}}^{r_i} \theta(r) r dr = \frac{1}{4} A_i \left(2(r_i)^2 \ln r_i - (r_i)^2 - 2(R^{(i-1)})^2 \ln R^{(i-1)} + (R^{(i-1)})^2 \right) + \frac{1}{2} B_i \left((r_i)^2 - (R^{(i-1)})^2 \right) \quad (88)$$

675 According to the boundary conditions and following continuity relationships, the unknown coefficients $C_1, C_2, \dots, C_{2n-1}, C_{2n}$ in Eq. (86) can be determined by Eq. (91).

Boundary condition :

$$\sigma_{r_1}|_{r_1=R^{(0)}} = 0; \quad \sigma_{r_1}|_{r_n=R^{(n)}} = 0$$

Stress continuity condition:

$$\begin{cases} \sigma_{r_1}|_{r_1=R^{(1)}} = \sigma_{r_2}|_{r_2=R^{(1)}} \\ \vdots \\ \sigma_{r_i}|_{r_i=R^{(i)}} = \sigma_{r_{i+1}}|_{r_{i+1}=R^{(i)}} \\ \vdots \\ \sigma_{r_{n-1}}|_{r_{n-1}=R^{(n-1)}} = \sigma_{r_n}|_{r_n=R^{(n-1)}} \end{cases} \quad (89)$$

Displacement continuity condition:

$$\begin{cases} u_{r_1}|_{r_1=R^{(1)}} = u_{r_2}|_{r_2=R^{(1)}} \\ \vdots \\ u_{r_i}|_{r_i=R^{(i)}} = u_{r_{i+1}}|_{r_{i+1}=R^{(i)}} \\ \vdots \\ u_{r_{n-1}}|_{r_{n-1}=R^{(n-1)}} = u_{r_n}|_{r_n=R^{(n-1)}} \end{cases} \quad (90)$$

$$\begin{bmatrix} \lambda_1 & -\frac{\eta_1}{(R^{(0)})^2} & 0 & & & & \\ \lambda_1 & -\frac{\eta_1}{(R^{(1)})^2} & -\lambda_2 & \frac{\eta_2}{(R^{(1)})^2} & & & \\ R^{(1)} & \frac{1}{(R^{(1)})^2} & -R^{(1)} & -\frac{1}{R^{(1)}} & & & \\ & \ddots & \ddots & \ddots & \ddots & & \\ & & \lambda_{n-1} & -\frac{\eta_{n-1}}{(R^{(n-1)})^2} & -\lambda_n & \frac{\eta_n}{(R^{(n-1)})^2} & \\ & & R^{(n-1)} & \frac{1}{R^{(n-1)}} & -R^{(n-1)} & -\frac{1}{R^{(n-1)}} & \\ & & & 0 & \lambda_n & -\frac{\eta_n}{(R^{(n)})^2} & \end{bmatrix} \begin{bmatrix} C_1 \\ C_2 \\ C_3 \\ \vdots \\ C_{2n-2} \\ C_{2n-1} \\ C_{2n} \end{bmatrix} = \begin{bmatrix} 0 \\ P_{T_1} \\ -u_{T_1} \\ \vdots \\ P_{T_{n-1}} \\ -u_{T_{n-1}} \\ P_{T_n} \end{bmatrix} \quad (91)$$

where

$$P_{T_i} = \frac{\theta}{(R^{(i)})^2} \int_{R^{(i-1)}}^{R^{(i)}} \theta(r) r dr; \quad u_{T_i} = \frac{\phi_i}{(R^{(i)})^2} \int_{R^{(i-1)}}^{R^{(i)}} \theta(r) r dr \quad (92)$$